Spin Properties of Transition-Metallorganic Self-Assembled Molecules

Prepared by:

Zhi Gang Yu, Senior Research Physicist
Applied Optics Laboratory

Prepared for:

Division of Materials Sciences and Engineering
SC -22.2 Basic Energy Sciences
U.S. Department of Energy
Germantown Building
1000 Independence Avenue, SW
Washington DC 20585-1290

Attention: Dr. James Davenport

Approved by:

Robert Brown, Director
Applied Optics Laboratory

Abstract

This report summarizes SRIs accomplishments on the project, "Spin Properties of Transition-Metallorganic Self-Assembled Molecules" funded by the Office of Basic Energy Sciences, U.S. Department of Energy (Grant No. DE-FG02-06ER46325). We have successfully carried out all tasks identified in our proposal and gained significant knowledge and understanding of spin-polarized electronic structure, spin relaxation, and spin-dependent transport in transition-metallorganic molecules and endohedral fullerenes. These molecules contain integrated spin and charge components and will enable us to achieve sophisticated functions in spintronics and quantum computing at molecular level with simple circuitry and easy fabrication. We have developed microscopic theories that describe the underlying mechanisms of spin-dependent processes and constructed quantitative modeling tools that compute several important spin properties. These results represent the basic principles governing the spin-dependent behaviors in nanostructures containing such molecules. Based on these results we have shown that novel device functions, such as electrically controlled g-factor and noninvasive electrical detection of spin dynamics, can be achieved in these nanostructures. Some of our results have been published in peer-reviewed journals and presented at professional conferences. In addition, we have established a close collaboration with experimentalists at Oxford University, UK (Dr. J. Morton and Prof. G. Briggs), Princeton University (Dr. A. Tyryshkin and Prof. S. Lyon), University of Delaware (Prof. E. Nowak), and University of California (Profs. R. Kawakami and J. Shi), who have been studying related systems and supplying us with new experimental data. We have provided our understanding and physical insights to the experimentalists and helped analyze their experimental measurements. The collaboration with experimentalists has also broadened our research scope and helped us focus on the most relevant issues concerning these materials.

1   Introduction

Organic molecules for charge transport, as in molecular wire junctions, or for magnetism, as in nanomagnets, are being extensively investigated. The stimulated quest for spin electronics and quantum computing renders it desirable to synthesize nanostructures with integrated spin and charge components. These nanostructures will enable us to achieve sophisticated functions with much simpler circuitry and less demanding fabrication. Among these nanostructures are transition-metallorganic self-assembled molecules (TMSAMs) and endohedral fullerenes. The localized electron spin at the central transition-metal ion or atom in such a molecule possesses quantum information, while the π-conjugated ligand or fullerene cage provides an efficient pathway for charge transport without spoiling the spin. Because of the unique synergy of spin, charge, and lattice in these molecules and their great potential in nanotechnology, the DOE Office of Basic Energy Sciences funded SRI International in Sepetember 2006 to conduct a theoretical research project to systematically and fundamentally study electronic and transport properties of these molecules, with emphasis on spin-related properties. We have successfully performed all the project tasks and developed microscopic theories and modeling tools to describe spin-polarized electronic structure, spin resonance and relaxation, and spin-dependent electrical transport in these molecules and device structures. Our achievements are described in detail below.

2   Spin states in TMSAMs and endohedral N@C$_{60}$

We have obtained the accurate electronic structure and optimized lattice configuration of representative transition-metal self-assembled molecules (TMSAMs) containing Fe^{3+} and Mn^{2+}, as shown in Fig. 1, and N@C$_{60}$, one of the most interesting endohedral fullerenes, as shown in Fig. 2, using two first-principles approaches, DMOL$_3$ and SIESTA.

2.1   TMSAMs

We have established a model Hamiltonian to describe spin states on Fe and Mn in these two TMSAMs based on the obtained first-principles electronic structure. Several important features in this Hamiltonian are as follows.

Strong ligand field regime. The interaction between the ligands and the metal ion breaks the five-fold degenerate d orbitals of Mn (II) into doubly degenerate e_g (d_{z^2} and $d_{x^2-y^2}$) states and triply degenerate t_{2g} states (d_{xy}, d_{yz}, and d_{xz}) with an energy separation Δ. The 5 d electrons in Mn (II) and Fe(III) can arrange themselves in two possible
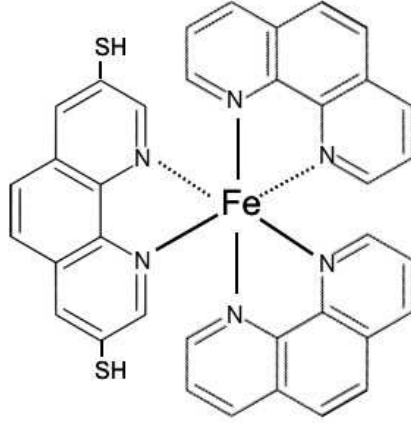
Figure 1: A representative conjugated metallorganic molecule containing an ion, Fe III. The surrounding ligands are phenanthroline, a strong ligand used in various complexes. One of the phenanthroline ligands is decorated by two dithiol (i.e., SH) groups at the ends for good contact with the electrodes.

configurations: one has a high spin of 5/2 if the exchange interaction of d electrons (Hunds rule) is stronger than the ligand field Δ; the other has a low spin of 1/2 with all 5 electrons occupying t_{2g} levels if the exchange interaction is much weaker than Δ. From the first-principles calculations we find that it is the latter scenario that occurs in this kind of molecule and that Δ is very large ($\Delta = 3.2$ eV for Fe^{3+} and 2.2 eV for Mn^{2+}), indicating that e_g states can be safely neglected in studying spin states in these TMSAMs.

Hole representation. We have noticed that 5 d electrons occupying 3 t_{2g} levels are equivalent to 1 hole in a closed t_{2g} shell. So instead of the conventional electron representation we use the hole representation, which greatly simplifies the Hamiltonian. In the hole representation, the spin-orbit coupling has the opposite sign compared to that in the electron representation.

Small splitting between t_{2g} levels. The octahedral symmetry of the ligand field is slightly broken in the TMSAM because one ligand has two (SH) groups but the other two ligands do not. A careful analysis indicates that this small difference can be described by a tetragonal distortion, which creates an energy splitting between d_{xy} and the degenerate d_{xz} and d_{yz}. From the first-principles results, the splitting in these molecules is about 0.02 eV.

Covalence π-bonding between d orbitals and p orbitals of N atoms. Our first-principles results suggest that there is considerable π-bonding between the Mn t_{2g} orbitals and p orbitals of the 6 N atoms surrounding the Mn ion. The p orbitals with t_{2g} symmetry were constructed and included as part of the basis set of the Hamiltonian.

Denoting $d_1 = d_{xy}$, $d_2 = d_{xz}$, $d_3 = d_{yz}$, and $\langle d_i|V_T|d_i\rangle = E_i$ for electrons, where V_T is the potential due to the ligands, and using the basis of $(d_i \uparrow, d_i \downarrow)$, we can write the Hamiltonian for the relevant spin states as

$$
H = \begin{pmatrix}
-E_1 + \mu_B H_z & \mu_B(H_x - iH_y) & -i\mu_B H_x & -\frac{i}{2}\xi & i\mu_B H_y & \frac{1}{2}\xi \\
\mu_B(H_x + iH_y) & -E_1 - \mu_B H_z & -\frac{i}{2}\xi & -i\mu_B H_x & -\frac{1}{2}\xi & i\mu_B H_y \\
i\mu_B H_x & \frac{i}{2}\xi & -E_2 + \mu_B H_z & \mu_B(H_x - iH_y) & -\frac{i}{2}\xi - i\mu_B H_z & 0 \\
\frac{i}{2}\xi & i\mu_B H_x & \mu_B(H_x + iH_y) & -E_2 - \mu_B H_z & 0 & \frac{i}{2}\xi - i\mu_B H_z \\
-i\mu_B H_y & -\frac{1}{2}\xi & \frac{i}{2}\xi + i\mu_B H_z & 0 & -E_3 + \mu_B H_z & \mu_B(H_x - iH_y) \\
\frac{1}{2}\xi & -i\mu_B H_y & 0 & -\frac{i}{2}\xi + i\mu_B H_z & \mu_B(H_x + iH_y) & -E_3 - \mu_B H_z
\end{pmatrix}.
$$

(2.1)

where ξ is the SO coupling, H_q ($q = x, y, z$) is the applied magnetic field, and mu_B the Bohr magneton.

2.2 N@C$_{60}$

Both experimental observations and first-principles calculations indicate that the electronic configuration of the N atom in N@C$_{60}$ retains its atomic form and that no chemical bonding between the N and the C$_{60}$ cage takes place. In the ground state of a free N atom, three $2p$ electrons align their spins in parallel according to Hund's rule, forming a degenerate quartet, ^4S, with total spin $S = 3/2$ and total orbital angular momentum $L = 0$. Its orbital wavefunction, in terms of single-electron $2p$ orbitals, is

$$
^4S = -\frac{1}{\sqrt{6}} \begin{vmatrix}
\phi_{-1}(1) & \phi_0(1) & \phi_1(1) \\
\phi_{-1}(2) & \phi_0(2) & \phi_1(2) \\
\phi_{-1}(3) & \phi_0(3) & \phi_1(3)
\end{vmatrix},
$$

(2.2)

where $\phi_1 = -\frac{1}{\sqrt{2}}(p_x + ip_y)$, $\phi_0 = p_z$, and $\phi_{-1} = \frac{1}{\sqrt{2}}(p_x - ip_y)$. Because of its zero orbital angular momentum, the SO interaction does not have any effect within the quartet.

To account for spin relaxation, one must consider the SO interaction between the ground state and excited states. The lowest excited states are doublets ($S = 1/2$), ^2P ($L = 1$) and ^2D ($L = 2$). For doublets ^2P and ^2D, without loss of generality, we assume electron 2 and 3 are spin-up and electron 1 is spin-down, and their orbital wavefunctions,
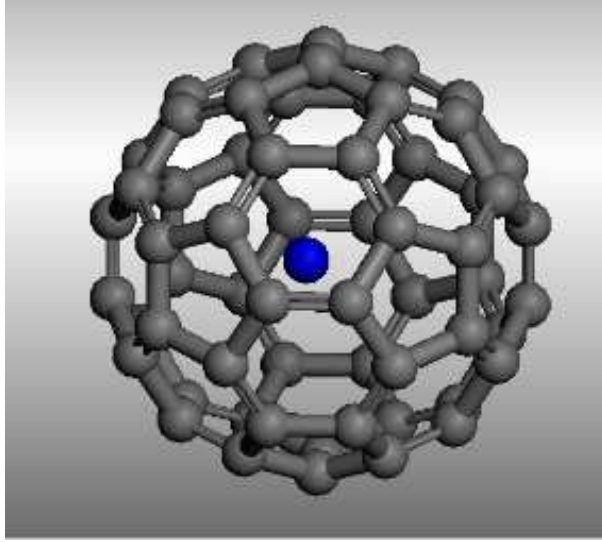
Figure 2: A representative endohedral fullerene, N@C$_{60}$, where a nitrogen atom with spin $3/2$ is located at the center of a C$_{60}$ cage.

^2L_m $(m = -L, -L+1, ..., L)$, can be written as

$$^2D_2 = \frac{1}{\sqrt{2}}\phi_1(1) \begin{vmatrix} \phi_0(2) & \phi_1(2) \\ \phi_0(3) & \phi_1(3) \end{vmatrix},\tag{2.3}$$

$$^2P_1 = \frac{1}{2}\phi_1(1) \begin{vmatrix} \phi_{-1}(2) & \phi_1(2) \\ \phi_{-1}(3) & \phi_1(3) \end{vmatrix} - \frac{1}{2}\phi_0(1) \begin{vmatrix} \phi_0(2) & \phi_1(2) \\ \phi_0(3) & \phi_1(3) \end{vmatrix}.\tag{2.4}$$

The orbital wavefunctions of other ^2D_m and ^2P_m can be obtained by applying the operator $\hat{L}_- = (\hat{L}_x - i\hat{L}_y)$ to $^2D_2$ and $^2P_1$.

Since N has a rather weak SO coupling, the SO interaction is aptly described by the LS scheme, where states are denoted as $^{2S+1}L_J^M$ with $J = |L-S|, ..., L+S$ and $M = -J, ..., J$. Hence through the SO coupling, S^4 forms $^4S_{3/2}$, ^2P forms $^2P_{3/2}$ and $^2P_{1/2}$, and ^2D forms $^2D_{5/2}$ and $^2D_{3/2}$,

$$^2P_{1/2(3/2)}^M = \sqrt{\frac{3/2 - (+)M}{3}}\, {}^2P_{M-1/2}^+ - (+)\sqrt{\frac{3/2 + (-)M}{3}}\, {}^2P_{M+1/2}^-,\tag{2.5}$$

$$^2D_{3/2(5/2)}^M = \sqrt{\frac{5/2 - (+)M}{5}}\, {}^2D_{M-1/2}^+ - (+)\sqrt{\frac{5/2 + (-)M}{5}}\, {}^2D_{M+1/2}^-,\tag{2.6}$$

where $^2L_m^{+(-)}$ denotes the up-spin (down-spin) state with an orbital ^2L_m.

The electronic Hamiltonian for the N $2p$ electrons is $H = U^+(H^0 + H_{SO})U$, where the basis set $U = ({}^4S_{\frac{3}{2}}, {}^2D_{\frac{3}{2}}, {}^2P_{\frac{3}{2}}, {}^2D_{\frac{5}{2}}, {}^2P_{\frac{1}{2}})^T$. H^0 describes the term energies of the ${}^4S$, ${}^2D$, and ${}^2P$,

$$H^0 = \begin{pmatrix} E_1 & 0 & 0 & 0 & 0 \\ 0 & E_2 & 0 & 0 & 0 \\ 0 & 0 & E_3 & 0 & 0 \\ 0 & 0 & 0 & E_2 & 0 \\ 0 & 0 & 0 & 0 & E_3 \end{pmatrix}, \tag{2.7}$$

where $E_1 = E_S$, $E_2 = E_D$, $E_3 = E_P$, and the SO interaction is

$$H_{SO} = \frac{1}{2}\zeta_p \begin{pmatrix} 0 & 0 & 2 & 0 & 0 \\ 0 & 0 & \sqrt{5} & 0 & 0 \\ 2 & \sqrt{5} & 0 & 0 & 0 \\ 0 & 0 & 0 & 0 & 0 \\ 0 & 0 & 0 & 0 & 0 \end{pmatrix}, \tag{2.8}$$

where ζ_p is the SO coupling strength for a single $2p$ electron. In the LS scheme, ${}^2P_{\frac{1}{2}}$ and ${}^2D_{\frac{5}{2}}$ are not mixed with states with $J = 3/2$. By diagonalizing the Hamiltonian, we obtain in the $J = 3/2$ manifold the three eigen-energies $\tilde{E}_i$ and eigenstates, denoted by ${}^{2S+1}\tilde{L}_J$, which is related to ${}^{2S+1}L_J$ through a transformation matrix K. In particular, the ground state is

$$ {}^4\tilde{S}_{\frac{3}{2}}^M = K_{11} \, {}^4S_{\frac{3}{2}}^M + K_{12} \, {}^2D_{\frac{3}{2}}^M + K_{13} \, {}^2P_{\frac{3}{2}}^M. \tag{2.9}$$

Hence these eigenstates ${}^{2S+1}\tilde{L}_J$ are not pure spin states and transitions between them will cause spin relaxation. Using the experimental values $E_D - E_S = 2.38$ eV, $E_P - E_S = 3.58$ eV, and $\zeta_p = 76$ cm^{-1} for a free N atom, we obtain $K_{11} = 1.0$, $K_{12} = 1.2 \times 10^{-5}$, $K_{13} = 2.6 \times 10^{-3}$, and $\tilde{E}_i \simeq E_i$.

3 Electron spin relaxation

3.1 TMSAMs

We have identified the spin relaxation mechanism in the TMSAM and developed a theoretical model to calculate spin relaxation times. The predominant spin relaxation mechanism is through orbit-lattice coupling between the t_{2g} electrons and the vibrational modes of the molecule. We supplement the obtained Hamiltonian described in Eq. (2.1) above
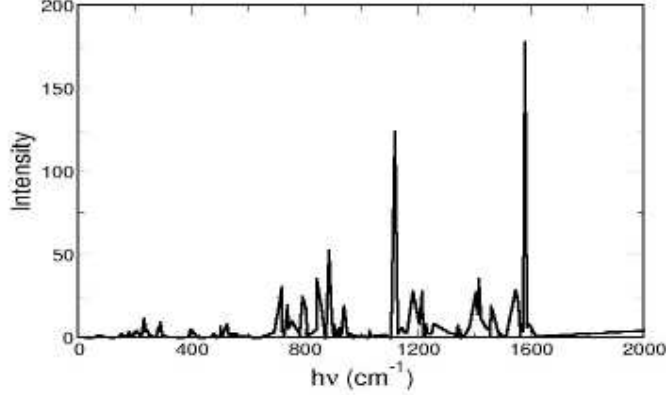
Figure 3: Distribution of vibrational frequencies in the TMSAM of Fig. 1.

with the following orbit-vibration coupling

$$
H_{OV} = g_1 \begin{pmatrix} 0 & \sqrt{2}Q_3 & -\sqrt{2}Q_2 \\ \sqrt{2}Q_3 & Q_3 & Q_2 \\ -\sqrt{2}Q_2 & Q_2 & -Q_3 \end{pmatrix} + g_2 \begin{pmatrix} 2Q_4 & Q_6 & Q_5 \\ Q_6 & -\sqrt{2}Q_6 - Q_4 & \sqrt{2}Q_5 \\ Q_5 & \sqrt{2}Q_5 & \sqrt{2}Q_6 - Q_4 \end{pmatrix},
$$
(3.1)

where Q_i $(i = 2, , 6)$ are relevant normal modes that contribute to the spin relaxation and g_1 and g_2 are the coupling strength. We consider H_{OV} as a perturbation but treat the spin-orbit interaction exactly, which goes beyond the work of Van Vleck, where both the spin-orbit and orbit-lattice interactions were treated perturbatively.

3.1.1 Phonon modes

We have carried out the first-principles calculations to obtain the frequencies of the vibrational modes in the TMSAM. The vibrational spectrum is plotted in Fig. 3. By analyzing the eigen-functions of normal vibrational modes, the frequencies of the relevant modes to spin relaxation are found to be between 200 cm^{-1} and 350 cm^{-1}.

3.1.2 Spin relaxation processes

Spin-lattice relaxation occurs through either the one-phonon (direct) process or the two-phonon (Raman) process. In the former, an up-spin electron (or hole) emits a phonon

and flips its spin, and the transition rate is

$$W \propto |\langle -|H_{OV}|+\rangle \delta(E_z - \hbar\omega), \tag{3.2}$$

where E_z is the Zeeman energy. In the latter, an up-spin electron (or hole) absorbs a phonon with frequency ω_1 and emits another phonon with frequency ω_2, and flips its spin. The probability of this transition can be calculated via

$$W \propto \Big| \sum_t \Big[\frac{\langle -|H_{OV}|t\rangle\langle t|H_{OV}|+\rangle}{E_+ - E_t + \hbar\omega_1} + \frac{\langle -|H_{OV}|t\rangle\langle t|H_{OV}|+\rangle}{E_+ - E_t - \hbar\omega_2} \Big] \Big|^2 \delta(E_z + \hbar\omega_1 - \hbar\omega_2) \tag{3.3}$$

where $|t\rangle$ denotes intermediate states. We emphasize that since $|+\rangle$, $|-\rangle$, and $|t\rangle$ are the exact eigenstates of our Hamiltonian that includes the spin-orbit interaction, they are not pure spin states, meaning that $|+\rangle$ ($|-\rangle$) contains a portion of down (up) spin states, which makes spin relaxation possible through the spin-independent H_{OV}. In a solid, both processes can be important to spin relaxation. In the TMSAMs, we find that the direct process is not functional, because the phonon energies of the 5 relevant modes in a TMSAM are all much larger than the Zeeman energy. Thus the Raman process is the only process that gives rise to spin relaxation. We have calculated the transition rate W of the Raman process in the TMSAM in Fig. 1. We find that the relaxation time can be expressed as

$$\frac{1}{T_1} = \sum_l A_l \frac{\exp(-\hbar\omega_l/k_B T)}{[1 - \exp(-\hbar\omega_l/k_B T)]^2}, \tag{3.4}$$

where ω_l ($l = 2,,6$) are the frequencies of the 6 relevant vibrational modes and A_l is a constant that does not depend on temperature.

3.2   N@C$_{60}$

We have developed a comprehensive microscopic model to describe both the spin relaxation time T_1 and the spin decoherence time T_2 in N@C$_{60}$ and quantitatively explained the experimentally measured T_1 and T_2. This is the first microscopic theory of electron spin relaxation in this type of nanostructure.

3.2.1   Orbit-vibration coupling

In N@C$_{60}$ the three $2p$ electron orbitals of a N atom at the center of C$_{60}$ transform like t_{1u} in the icosahedral group I_h. According to the Jahn-Teller theorem, $t_{1u} \otimes t_{1u} = A_g \oplus T_{1g} \oplus H_g$, they can couple only to vibrations with these three representations. Among

them the total symmetric A_g and antisymmetric T_{1g} are ineffectual because the former cannot break the degeneracy of $2p$ orbitals, and the latter cannot couple. C_{60} has eight $H_g(k)$ branches ($k = 1, .., 8$) and each branch is five-fold degenerate in energy. We focus only on the lowest branch, $k = 1$, since other H_g modes have much higher energies and are not much excited at room temperature. The orbital-vibration coupling between the p_q orbital and the five H_g modes, Q_i ($i = 1, ..., 5$) is

$$H_{OV} = \frac{1}{2}g \begin{pmatrix} Q_5 - \sqrt{3}Q_4 & -\sqrt{3}Q_1 & -\sqrt{3}Q_2 \\ -\sqrt{3}Q_1 & Q_5 + \sqrt{3}Q_4 & -\sqrt{3}Q_3 \\ -\sqrt{3}Q_2 & -\sqrt{3}Q_3 & -2Q_5 \end{pmatrix}, \tag{3.5}$$

where g is the coupling strength.

3.2.2 Coupling strength g

We estimate the coupling strength g by setting $Q_i = 0$ for $i = 1 - 4$ and a nonzero $Q_5 = \delta Q(3\cos^2\theta - 1)$ with θ being the polar angle, and evaluating the energy change of a N $2p$ electron. The $2p$ electron wavefunctions in a free N atom are

$$|2p_z\rangle = \frac{1}{\sqrt{\pi}} \alpha_0^{5/2} r e^{-\alpha_0 r} \cos\theta \tag{3.6}$$

$$|2p_x\rangle = \frac{1}{\sqrt{\pi}} \alpha_0^{5/2} r e^{-\alpha_0 r} \sin\theta \cos\phi, \tag{3.7}$$

where $\alpha_0 = Z^*/2a_0$, a_0 is the Bohr radius, and $Z^* = 3$ is the valence charge. These wavefunctions are the eigenstates of a Schrödinger equation with a Coulomb potential $(-e)V_0 = -Z^*e^2/r$ in a free space.

In the presence of C_{60}, the boundary condition and the potential will change. To the $2p$ electrons, the C_{60} cage is essentially a cavity with $r_0 = 1.74$ Å in a dielectric medium. The nonzero Q_5 makes the C_{60} sphere shrink along one direction but elongate along the other two normal directions, resulting in an ellipsoid described by the equation $\rho^2/a^2 + z^2/c^2 = 1$, where $\rho^2 = x^2 + y^2$, $c = r_0 - 2\delta Q$, and $a = r_0 + \delta Q$. The potential created by a point charge Z^*e at the center of such an ellipsoidal cavity is

$$V_1 = \begin{cases} \frac{Z^*e}{\sqrt{a^2-c^2}} \tan^{-1} \sqrt{\frac{a^2-c^2}{\xi+c^2}} & : \quad a^2 - c^2 < \xi < 0 \\ \frac{Z^*e}{\epsilon\sqrt{a^2-c^2}} \tan^{-1} \sqrt{\frac{a^2-c^2}{\xi+c^2}} & : \quad \xi > 0, \end{cases} \tag{3.8}$$

where ξ and η are ellipsoidal coordinates, which are related to the Cartesian coordinates through $x = \sqrt{\frac{(\xi+a^2)(\eta+a^2)}{a^2-c^2}} \cos\phi$, $y = \sqrt{\frac{(\xi+a^2)(\eta+a^2)}{a^2-c^2}} \sin\phi$, $z = \pm\sqrt{\frac{(\xi+c^2)(\eta+c^2)}{c^2-a^2}}$, and ϕ is the azimuthal angle.

9

The energy changes of the $2p$ electrons due to $\delta V \equiv V_1 - V_0$ are $\delta E_q = \langle 2p_q| -e\delta V |2p_q\rangle$, and the coupling strength is $g = \frac{1}{2}\frac{\delta E_z - 2\delta E_x}{\delta Q}$. We obtain $g = 1.4$ eV/Å for $\epsilon = 5$ and $g = 1.37$ eV/Å for $\epsilon = 4.5$. It is noted that this value is considerably larger than the coupling between a C π-electron and the vibrations in C_{60}, but similar to the displacement derivative of electrostatic energy of an electron centered in a C_{60} cage, $\simeq 1$ eV/Å, from *ab initio* calculations.

3.2.3 Effective spin Hamiltonian

For spin relaxation, the energy loss due to spin flip must be dissipated into a local environment. Since the energy involved in spin flips is $\sim 10^{-5}$ eV with a Larmor frequency at 9.7 GHz, whereas the lowest energy of C_{60} vibrations is about 30 meV, it is impossible to flip a spin by absorbing or emitting a single C_{60} vibration quanta (one-phonon process). One must consider a higher-order Raman process. Using the second-order perturbation of H_{OV}, we derive an effective Hamiltonian between the ground-state quartets, $^4\tilde{S}^i_{\frac{3}{2}}$,

$$
\begin{aligned}
\langle^4\tilde{S}^i_{\frac{3}{2}}|H_{eff}|^4\tilde{S}^j_{\frac{3}{2}}\rangle &= \sum_{\mu\nu}\Big(\sum_{LJM}\frac{\langle^4\tilde{S}^i_{\frac{3}{2}},n_\mu^- n_\nu^+|H_{OV}|LJM,n_\mu^- n_\nu\rangle\langle LJM,n_\mu^- n_\nu|H_{OV}|\ ^4\tilde{S}^j_{\frac{3}{2}},n_\mu n_\nu\rangle}{E_S - E_{LJ} - \hbar\omega_\mu} \\
&+ \sum_{LJM}\frac{\langle^4\tilde{S}^i_{\frac{3}{2}},n_\mu^- n_\nu^+|H_{OV}|LJM,n_\mu n_\nu^+\rangle\langle LJM,n_\mu n_\nu^+|H_{OV}|^4\tilde{S}^j_{\frac{3}{2}},n_\mu n_\nu\rangle}{E_S - E_{LJ} + \hbar\omega_\nu}\Big) (3.9)
\end{aligned}
$$

where n_μ is the phonon number of the μth mode, ω_μ is its frequency, and $n_\mu^\pm = n_\mu \pm 1$. The intermediate states $|LJM\rangle$ include all $\tilde{D}^M_{\frac{3}{2}}$, $\tilde{P}^M_{\frac{3}{2}}$, $D^M_{\frac{5}{2}}$, and $P^M_{\frac{1}{2}}$. Since $|E_S - E_{LJ}| > 2$ eV $\gg \hbar\omega_\mu \equiv \hbar\omega \simeq 30$ meV, the energy of the H_g modes, we can safely neglect $\hbar\omega_\mu$ in the denominators in Eq. (3.9). After a lengthy calculation, we find the fluctuating Hamiltonian $H_I(t) = H_{eff} - \overline{H_{eff}}$ ($\overline{A}$ is the time average of A) due to C_{60} H_g vibrations can be summarized in terms of spin operators

$$
\begin{aligned}
H_I(t) &= \gamma\Big[(\lambda_1 - \bar{\lambda}_1)\Big(\hat{S}_z^2 - \frac{5}{4}\Big) + (\lambda_2 - \bar{\lambda}_2)(\hat{S}_+\hat{S}_z + \hat{S}_z\hat{S}_+ \\
&+ \hat{S}_-\hat{S}_z + \hat{S}_z\hat{S}_-) + (\lambda_3 - \bar{\lambda}_3)(\hat{S}_+^2 + \hat{S}_-^2)\Big],
\end{aligned} \tag{3.10}
$$

$$\gamma = \frac{K_{12}^2}{E_S - E_P} - \frac{5}{3}\frac{K_{13}^2}{E_S - E_D},$$

$$\lambda_1 = \frac{9g^2}{40}(4Q_1^2 - Q_2^2 - Q_3^2 + 4Q_4^2 - 4Q_5^2),$$

$$\lambda_2 = -\frac{3g^2}{40}[3(Q_2 + iQ_3)(Q_4 - iQ_1) + \sqrt{3}Q_5(Q_2 - iQ_3)],$$

$$\lambda_3 = \frac{3g^2}{80}[4\sqrt{3}Q_5(Q_4 - iQ_1) - 3(Q_2 - iQ_3)(Q_2 - iQ_3)],$$

where $Q_\mu = (\frac{f\hbar}{M\omega})^{1/2}(a_\mu + a_\mu^\dagger)$, $M = 60M_C$ with M_C being the mass of the C atom, $a_\mu^\dagger$ is the phonon creation operator for the μth mode, and $f = \sqrt{5}/2$ is the normalization factor for H_g modes.

3.2.4 Spin relaxation time T_1

In a system with a definable spin temperature, the spin relaxation time T_1 can be calculated from

$$T_1^{-1} = \sum_{\xi\eta} W_{\xi\eta}(E_\xi - E_\eta)^2/2\sum_\eta E_\eta^2, \tag{3.11}$$

where E_ξ is the energy of state ξ in the presence of an applied magnetic field and $W_{\xi\eta}$ is the transition rate from ξ to η,

$$W_{\xi\eta} = \frac{2\pi}{\hbar}\overline{|\langle\eta|H_I(t)|\xi\rangle|^2}\rho(E). \tag{3.12}$$

with $\rho(E)$ being the density of final states in energy. For the vibrational excitations with a line width Γ,

$$\rho(E) = \frac{\hbar\Gamma}{2\pi}[E^2 + (\hbar\Gamma/2)^2]^{-1}. \tag{3.13}$$

The transition rate in Eq. (3.2) can be equivalently expressed in terms of temporal correlation functions,

$$W_{\xi\eta} = \int_{-\infty}^{+\infty}\frac{e^{i\omega_{\xi\eta}\tau}}{\hbar^2}\overline{\langle\xi|H_I(t)|\eta\rangle\langle\eta|H_I(t-\tau)|\xi\rangle}d\tau, \tag{3.14}$$

where $\hbar\omega_{\xi\eta} = E_\xi - E_\eta$. For a commonly used correlation time assumption, $\overline{H_I(t)H_I(t-\tau)} = \overline{|H_I(t)|^2}e^{-|\tau|/\tau_c}$, the two transition rate expressions are identical if $\Gamma = 2/\tau_c$. In the motional narrowing regime, $\hbar\Gamma > 2E$, we obtain the expression of T_1,

$$\frac{1}{T_1} = 2w \equiv \frac{567}{8}\gamma^2\frac{g^4}{(M\omega)^2\Gamma}\frac{e^{-\beta\hbar\omega}}{(1 - e^{-\beta\hbar\omega})^2}. \tag{3.15}$$
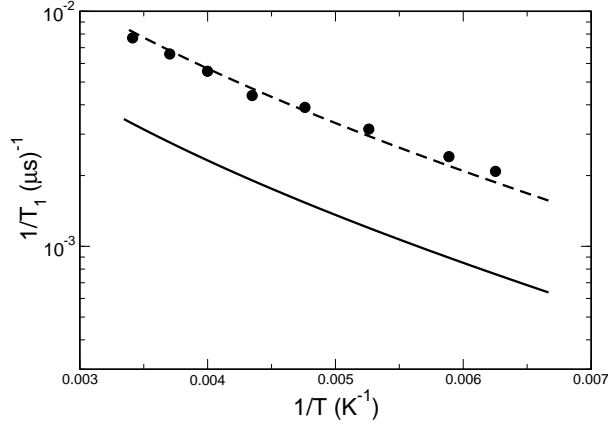
11

Figure 4: Logarithm of $1/T_1$ against $1/T$. Circles are measured data of N@C_{60} Solid line is our theoretical results with $\hbar\omega = 30$ meV, $g = 1.4$ eV/Å, and $\hbar\Gamma = 10^{-4}$ meV (corresponding to a lifetime of 10 ps). The dashed line is obtained by multiplying the solid line by a constant 2.46.

Figure 4 compares the measured T_1 of N@C_{60} in a non-polar CS_2 solvent with results from Eq. (3.15). We see an excellent agreement between theory and experiment. The factor of 2.5 difference is considered to be rather small in spin relaxation studies, and may be attributed to the fact that the N properties in N@C_{60} may slightly deviate from its free atomic values.

3.2.5 Spin decoherence time T_2

Experiments suggest that the system may have more than one T_2 constant. To identify all possible T_2, we solve the Redfield equation in the interaction representation,

$$d\mathcal{S}^*_{\xi\xi'}/dt = \sum_{\eta\eta'} R_{\xi\xi',\eta\eta'}\mathcal{S}^*_{\eta\eta'}, \tag{3.16}$$

12

where $\mathcal{S}^*_{\xi\xi'} \equiv \langle\xi|\hat{S}^*_x|\xi'\rangle$ and $\hat{S}^*_x(t) = e^{-i\frac{\mathcal{H}_0 t}{\hbar}}\hat{S}_x(t)e^{i\frac{\mathcal{H}_0 t}{\hbar}}$. $\mathcal{H}_0$ is the time-independent Zeeman term that determines spin resonance frequency and the Redfield matrix is

$$
\begin{aligned}
R_{\xi\xi',\eta\eta'} &= \frac{1}{2\hbar^2}\Big[J_{\xi\eta\xi'\eta'}(\omega_{\xi'\eta'}) + J_{\xi\eta\xi'\eta'}(\omega_{\xi\eta}) \\
&\quad - \delta_{\xi'\eta'}\sum_\zeta J_{\zeta\eta\zeta\xi}(\omega_{\zeta\eta}) - \delta_{\xi\eta}\sum_\zeta J_{\zeta\xi'\zeta\eta'}(\omega_{\zeta\eta'})\Big], \\
J_{\xi\xi'\eta\eta'}(\omega) &= \int_{-\infty}^{+\infty}\overline{\langle\xi|H_I(t)|\xi'\rangle\langle\eta'|H_I(t-\tau)|\eta\rangle}e^{-i\omega\tau}d\tau.
\end{aligned}
$$

Focusing on $\eta - \eta' = 1$ and denoting $X_1 = \mathcal{S}^*_{\frac{3}{2}\frac{1}{2}}$, $X_2 = \mathcal{S}^*_{\frac{1}{2}-\frac{1}{2}}$, $X_3 = \mathcal{S}^*_{-\frac{1}{2}-\frac{3}{2}}$, we obtain the general solution of normalized $\mathbf{X}(t)$,

$$
\mathbf{X}(t) = C_1\mathbf{U}_1 e^{-t/T'_{2o}} + C_2\mathbf{U}_2 e^{-t/T''_{2o}} + C_3\mathbf{U}_3 e^{-t/T_{2i}}, \tag{3.17}
$$

where $\mathbf{U}_1 = (1,0,1)^T/\sqrt{2}$, $\mathbf{U}_2 = (1,0,-1)^T/\sqrt{2}$, $\mathbf{U}_3 = (0,1,0)^T$, and C_i ($\sum_i |C_i|^2 = 1$) are coefficients determined by the initial condition. $T'_{2o} = 1/4w = T_1/2$ and $T''_{2o} = 1/2w = T_1$ are two independent T_2 constants for outer transitions and $T_{2i} = 1/2w = T_1$ is the T_2 constant for inner transitions. In the literature a single T_2 time is always assumed for the outer transitions. Our results suggest that new experiments and data extraction schemes are needed to resolve multiple T_2 constants. The measured T_{2i} is similar to but smaller than T_1 ($T_{2i} \simeq 0.7T_1$) and this discrepancy may be explained by the motional narrowing approximation used in the theory. Figure 5 compares the measured T_{2o}^{-1} and ratio T_{2i}/T_{2o} with the theory and shows good agreements. The excellent agreement on the ratio, which is independent of model parameters, is particularly remarkable.

This microscopic theory consistently explains recently measured T_1 and T_2 and their temperature dependence and predicts additional T_2 constants in N@C$_{60}$, suggesting a universal importance of the two-phonon Raman process in nanostructures. The complete microscopic theory was published in the paper, "Microscopic theory of electron spin relaxation in N@C60", *Phys. Rev. B* **77**, 205439 (2008).

4   Magnetic-field effect on electron spin relaxation in N@C$_{60}$

Our experimental collaborators at Oxford and Princeton measured spin relaxation T_1 and T_2 at 35 GHz (Q-band), 3.7 GHz (S band), and 100 GHz (W-band) (the corresponding magnetic fields being about 3.6 T, 0.1 T, 10 T) and found that spin relaxation in N@C$_{60}$
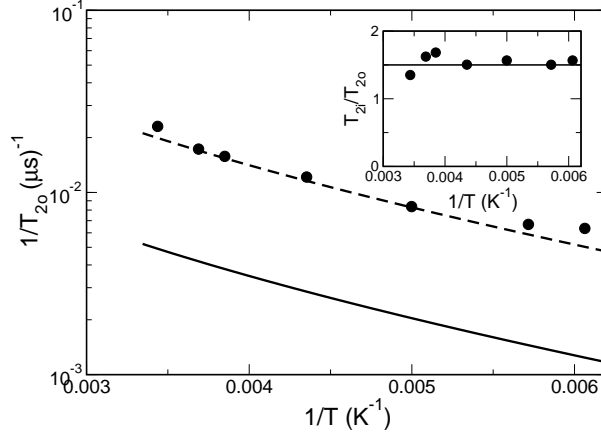
Figure 5: Logarithm of $1/T_{2o}$ against $1/T$. Circles are measured values and the solid line is our theoretical results. The dashed line is obtained by multiplying the solid line by a constant 4.0. The inset shows the ratio of T_{2i}/T_{2o} from experiment (circles) and theory (solid line).

strongly depends on the magnetic field and that the dependence cannot be explained by a mere Zeeman-energy change in the system. In light of the experimental observation, we have also studied the magnetic-field effect on electron spin relaxation to explain the experiments.

According to the microscopic theory described in the previous section, the excited state ^2P and ^2D play a central role in spin relaxation. After taking into account the spin-orbit coupling, these states can be grouped by the total angular momentum $J = L + S$. For example, ^2P states form $^2P_{1/2}$ with $J = 1/2$, and $^2P_{3/2}$ with $J = 3/2$. In the absence of magnetic field, states with different J values do not mix. In the presence of a magnetic field, however, J is no longer a good quantum number, but the magnetic quantum number m_J ($m_J = -J, -J+1, , J$) still is. Thus states $^2P_{1/2}$ and $^2P_{3/2}$ with a same m_J ($m_J =?1/2, 1/2$) mix with each other. The amount of admixture is determined by the relative importance of the Zeeman energy caused by the magnetic field and the energy splitting between states with different J (spin-orbit coupling). For a free N atom, the energy splitting between $^2P_{3/2}$ and $^2P_{1/2}$ from experiment is unusually small, 0.386 cm$^{?1}$, corresponding to 11.57 GHz. Hence for the Q-band and W-band experiments, this mixing becomes so significant that our theory becomes inadequate. The magnetic-field effect described above is essentially the Paschen-Back effect in atomic physics, where a strong magnetic field disrupts the coupling between the orbital and spin angular momenta, resulting in a different pattern of splitting than that under a weak magnetic field, where

14

the spin-orbit coupling is dominant. However, this effect is rarely seen in condensed matters because of their large spin-orbit couplings. It is interesting to note that N@C$_{60}$ provides such an unusual platform that bridges atomic physics and condensed matter physics.

To assess the magnetic-field effect on spin relaxation and decoherence in N@C$_{60}$, we incorporate the mixing among states with different J values in our microscopic model for spin relaxation. For example, the true eigen states for $P_{3/2}$ and $P_{1/2}$ would be

$$\tilde{P}_{3/2}^{1/2} = \cos\theta_1 P_{3/2}^{1/2} + \sin\theta_1 P_{1/2}^{1/2}, \tag{4.1}$$

$$\tilde{P}_{3/2}^{-1/2} = \cos\theta_2 P_{3/2}^{-1/2} + \sin\theta_2 P_{1/2}^{-1/2}, \tag{4.2}$$

where

$$\tan 2\theta_1 = \frac{2\sqrt{2}\hbar\omega_s}{\hbar\omega_s + 6\Delta}, \tag{4.3}$$

$$\tan 2\theta_2 = \frac{2\sqrt{2}\hbar\omega_s}{-\hbar\omega_s + 6\Delta}, \tag{4.4}$$

$\omega_s/2\pi$ is the electron spin resonance frequency, and $\Delta = 0.386$ cm^{-1} is the splitting between $^2P_{3/2}$ and $^2P_{1/2}$. The effective spin Hamiltonian needs modification to accommodate the magnetic-feild-induced mixing between $^2P_{1/2}$ and $^2P_{3/2}$, $H_I \to H_I(t) + H_I'(t)$, with

$$\begin{aligned}
H_I'(t) &= \gamma\Big[(\lambda_1' - \bar{\lambda}_1')\Big(\hat{S}_z^2 - \frac{9}{4}\Big) + 2\sqrt{2}(\lambda_2 - \bar{\lambda}_2)[\hat{S}_+(\hat{S}_z^2 - 1) + (\hat{S}_z^2 - 1)\hat{S}_+ \\
&+ \hat{S}_-(\hat{S}_z^2 - 1) + (\hat{S}_z^2 - 1)\hat{S}_-] + 2\sqrt{2}(\lambda_3 - \bar{\lambda}_3)(\hat{S}_+^2\hat{S}_z + \hat{S}_z\hat{S}_+^2 + \hat{S}_-^2\hat{S}_z + \hat{S}_z\hat{S}_-^2)\Big] \tag{4.5}
\end{aligned}$$

Using $H_I(t)$ and $H_I'(t)$, we express the electron spin relaxation time T_1 for N@C$_{60}$ as

$$\frac{1}{T_1} = \frac{1}{5}\Big[W_{\frac{3}{2}\frac{1}{2}} + W_{\frac{1}{2}-\frac{1}{2}} + W_{-\frac{1}{2}-\frac{3}{2}} + 4(W_{\frac{3}{2}-\frac{1}{2}} + W_{\frac{1}{2}-\frac{3}{2}})\Big], \tag{4.6}$$

where

$$W_{\frac{3}{2}\frac{1}{2}} = w_0(1 + t_1/\sqrt{2})^2 \frac{\Gamma}{\omega_s^2 + (\Gamma/2)^2} \tag{4.7}$$

$$W_{\frac{1}{2}-\frac{1}{2}} = \frac{3}{2}w_0(t_1 + t_2)^2 \frac{\Gamma}{\omega_s^2 + (\Gamma/2)^2} \tag{4.8}$$

$$W_{-\frac{1}{2}-\frac{3}{2}} = w_0(1 - t_2/\sqrt{2})^2 \frac{\Gamma}{\omega_s^2 + (\Gamma/2)^2} \tag{4.9}$$

$$W_{\frac{3}{2}-\frac{1}{2}} = w_0(1 - t_2\sqrt{2})^2 \frac{\Gamma}{4\omega_s^2 + (\Gamma/2)^2} \tag{4.10}$$

$$W_{\frac{1}{2}-\frac{3}{2}} = w_0(1 + t_1\sqrt{2})^2 \frac{\Gamma}{4\omega_s^2 + (\Gamma/2)^2} \tag{4.11}$$

15

where

$$w_0 = \frac{567}{64}\gamma^2 \frac{g^4}{M\omega} \frac{e^{-\beta\hbar\omega}}{(1 - e^{-\beta\hbar\omega})^2}, \tag{4.12}$$

and $t_1 = \tan\theta_1$ and $t_2 = \tan\theta_2$. We use Eq. (4.6) to fit the experimental data and find that $\Gamma = 2\pi \times 20$ GHz can explain the experimentally observed magnetic field dependence of spin relaxation time in N@C$_{60}$. This theory, together with related experimental measurements, is being written as a manuscript for publication.

5 Polaron formation in TMSAMs

We have established a tight-binding Hamiltonian for the ligand (as shown in Fig. 6) based on the first-principles electronic and lattice structures, in which each C, N, and S atom contributes one π electron,

$$
\begin{aligned}
H_L &= -\sum_{<ij>s} t_{ij}(c_{is}^\dagger c_{js} + \text{H.c.}) + \sum_i \left[\epsilon_i c_{is}^\dagger c_{is} + U_i n_{i\uparrow} n_{i\downarrow} \right] \\
&+ \sum_{<ij>} \frac{K}{2}(u_i - u_j)^2 + \frac{J}{2}\sum_s (c_{N_1 s}^\dagger \boldsymbol{\sigma}_{ss'} c_{N_1 s} \cdot \boldsymbol{S} + .c_{N_2 s}^\dagger \boldsymbol{\sigma}_{ss'} c_{N_2 s} \cdot \boldsymbol{S})
\end{aligned} \tag{5.1}
$$

Here $c_{is}^\dagger$ creates a π-electron with spin s at atomic site i, t_{ij} is the electron hopping between nearest neighboring site i to site j. The electron-lattice coupling is included by assuming that the hopping integral across a bond depends on the bond-length $t_{ij} = t_0[1 - \alpha(u_i - u_j)]$, where u_i is the displacement of the ith atom. The σ-bond between two adjacent atoms in the ligand are described by a bond-streching spring with an elastic constant K. The second term describes the energy of the π-orbital at each atom. The on-site Coulomb interaction is included in the fourth terms. The last term describes the magnetic coupling between electron spins in the N atoms and in the transition-metal ion, which is originated from the covalence π-bonding between transition-metal d orbitals and p orbitals of the N atoms. Based on our first-principles calculations, the parameters in the above Hamiltonian are estimated to be $\alpha = 5$ eV/Å, $K = 32$ eV/Å^2, $U = 1$ eV, $t_0 = 1.7$ eV, and $J_0 = 0.1$ eV. The site energies, ϵ_i, for C, N, and S are set 0, -0.8 eV, and 1.3 eV, respectively, which were extracted from systematic local-density functional studies of conjugated polymers.

We have studied polaron formation in the ligand by solving the obtained Hamiltonian. In this system, because of the strong electron-lattice interaction, an excess electron will be accompanied by a lattice distortion, forming a self-trapped polaron. The magnetic coupling between transition-metal ion and N π-electrons gives rise to spin-dependent polarons. Consequently, the spin distribution of the excess carrier is sensitive to the interplay
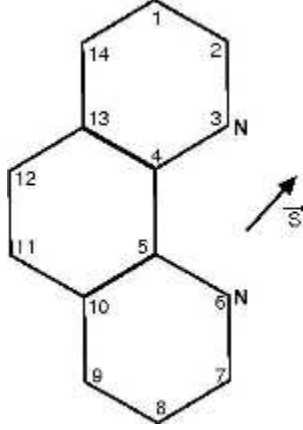
Figure 6: A conjugated ligand coupled with a transition-metal ion. C and N atoms in the ligand are labeled.

of the electron-lattice interaction and the magnetic coupling. From Fig. 7, we see that the electron-lattice interaction can significantly modify the spatial spin-density distribution. With increase of the electron-lattice interaction, the high spin-density regions can shift from the N atoms to C atoms.

We have identified the lowest up-spin and down-spin polaron levels and studied how their energies depend on the interplay of the electron-lattice and magnetic interactions. For a system without the magnetic coupling, the up-spin and down-spin polaron states are always degenerate in energy. The energy splitting between up-spin and down-spin polarons can be exploited to make devices using the spin degree of freedom. Figure 8 shows this energy splitting as a function of the magnetic coupling J for different electron-lattice interaction strengths. We see that the electron-lattice interaction in general reduces this energy splitting, leading to a smaller effective magnetic coupling.

6 Electrically controlled g-factor in TMSAMs

For a free transition-metal ion, because of its spin-orbit (SO) interaction, the total angular momentum, j ($j = l + s$, $l + s - 1$, ..., $|l - s|$, with l and s being orbital and spin angular momenta), is a good quantum number to characterize an eigenstate, which will be split up into $2j + 1$ sublevels with an equal spacing, $g\mu_B H$, upon the application of a magnetic field, H, where g is the Landé g-factor,

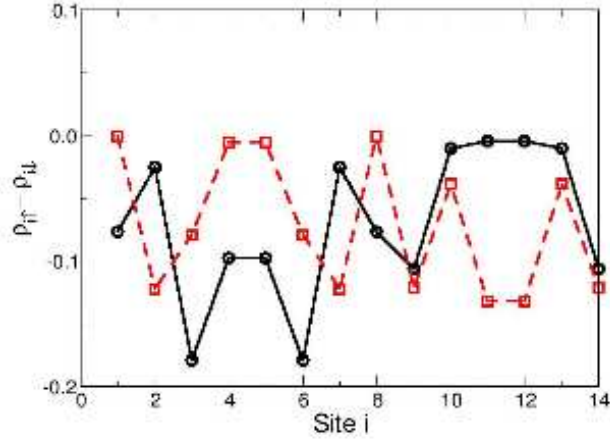$$g = 1 + \frac{j(j+1) - l(l+1) + s(s+1)}{2j(j+1)}.$$ (6.1)

17

Figure 7: Spin density on each atom with site labels described in Fig. 6. Circles and squares are for $\alpha = 0$ and 5 Å^{-1}, respectively. The magnetic coupling $J = 0.1$ eV.
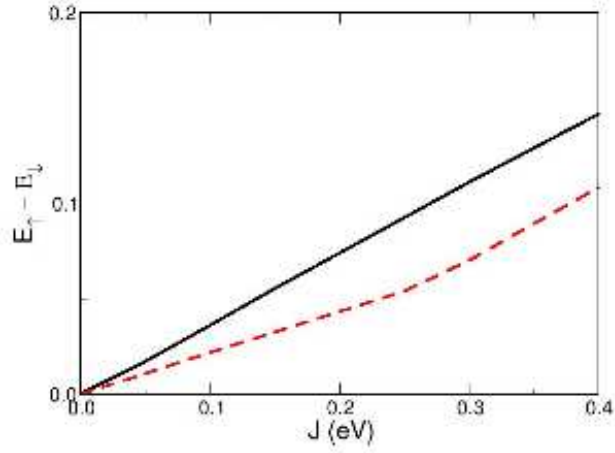

Figure 8: Energy difference between the lowest up-spin and down-spin polaron levels as a function of the magnetic coupling. Solid and dashed lines correspond to $\alpha = 0$ and 5 Å^{-1}, respectively.

18

The g-factor determines the ion's magnetic properties including the magnetic moment of each sublevel, $-g\mu_B m_j$ $(m_j = -j, ..., j)$, and the electron spin resonance frequency, $\omega = |g|\mu_B H/\hbar$.

A metal ion in a compound, however, can exhibit multifarious magnetic behaviors because the magnetic moment and g-factor can be strongly influenced by the local environment. Here we show that in a conjugated metallorganic molecule the magnetism and g-factor can be electrically tuned to a great extent, by modifying the charge distribution in one of the ligands. The capability of controlling the g-factor and magnetism at the molecular level will enable simple and versatile manipulation of individual electron spins.

We examine how the g-factor and magnetism change when the three t_{2g} orbitals have slightly different energies. To see the interplay of the SO coupling and the energy splitting among t_{2g} states more clearly, for simplicity we assume that d_{xy} always resides at the middle of d_{xz} and d_{yz} in energy, $\delta = E_2 - E_1 = E_1 - E_3$. The SO coupling of Fe(III) is fixed $\xi = -300$ cm^{-1}. We obtain the magnetic properties of the system by diagonalizing the Hamiltonian Eq. (2.1) at a small magnetic field (linear response).

Since the system has an odd number of electrons, according to Kramer's theorem, the six eigenstates in this system can be grouped into three Kramer's doublets, ψ_{2k-1} and ψ_{2k} $(k = 1, 2, 3)$, which is split upon the application of magnetic field H_ν along the ν-axis $(\nu = x, y, z)$ with an energy difference of $g_k^\nu \mu_B H_\nu$. The magnetic moments of each doublet, accordingly, have the same magnitude but are opposite in sign, $\mu_{2k-1}^\nu = -\mu_{2k}^\nu = g_k^\nu \mu_B/2$, where $\mu_k^\nu = \mu_B\langle\psi_k|l_\nu + 2s_\nu|\psi_k\rangle$. In Fig. 9, we plot the energies and $|g_k^\nu|$ for the three doublets as a function of the energy splitting factor, δ. We see that the g-factor can be dramatically modified, from 0 to over 3, within a relatively small δ change of 0.1 eV. In addition, g^x (g^y) becomes 0 at a finite δ for both the ground and excited states, as shown in Figs. 9(c) and 9(d), indicating that the system with that δ cannot be magnetized when the magnetic field is along the x (y) axis.

To further understand the g-factor change, we plot in Fig. 10 the contributions from the orbital and spin angular momenta to the magnetic momentum along the magnetic field direction for both the ground and excited states. When $|\delta| > |\xi| = 0.03$ eV, where the energy splitting dominates over the SO coupling, the increase of δ always diminishes the magnitude of the orbital, $|\langle l_\nu \rangle|$, which is the so-called orbital quenching due to the energy splittings. Meanwhile the spin keeps increasing, approaching $1/2$, its free-electron value. Consequently the g-factor approaches 2 and becomes isotropic when δ is large. When $|\delta| < |\xi|$, however, the dependences of spin and orbital on δ become more complicated. In this regime, the SO interaction, which connects states with different orbitals and spins, can partially reinstate the orbital angular momentum and meanwhile suppress the spin from its free-electron value. Compared to $\langle l_z \rangle$ and $\langle s_z \rangle$, $\langle l_x \rangle$ and $\langle s_x \rangle$ change more dramatically as δ varies, as shown in Figs. 10(c) and 10(d). In particular, a discontinuity, where both
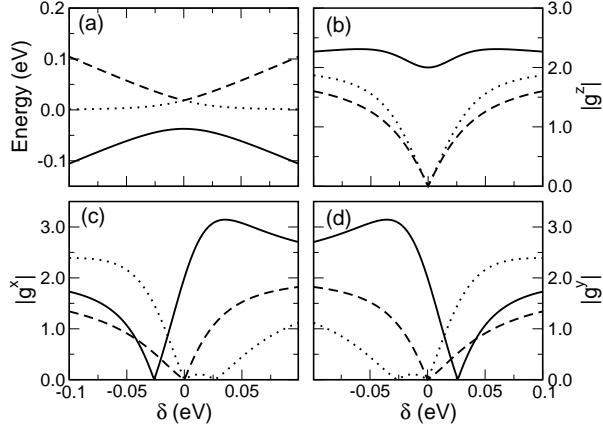
Figure 9: Energy (a), $|g^z|$ (b), $|g^x|$ (c), and $|g^y|$ (d) of the eigenstates as a function of energy splitting δ between t_{2g} levels. Solid, dotted, and dashed lines correspond to the ground state and the first and second excited states, respectively. The SO coupling is $\xi = -300$ cm^{-1}.

the spin and the orbital change their signs, occurs when g^x or g^y becomes zero at the finite δ.

The energies of the t_{2g} orbitals, E_i, ultimately come from the interaction between the ion and ligands, and particularly the excess charges on the N atoms surrounding the ion. The charges on the N atoms can be modified by applying a gate voltage across the ligand with the dithiol groups. To demonstrate this, we solve Hamiltonian Eq. (5.1) for the ligand self-consistently by using the unrestricted Hartree-Fock approximation. The excess charges in the two N atoms for $V = 0$ are found to be equal, $-0.12|e|$, where e is the electron charge, according to the first-principles calculations. The four N atoms in the other two ligands also have this excess charge, which remains constant and independent to V. In Fig. 11, we plot the result for the case where the electrostatic potential in the ligand depends on V in a simple linear form, $\epsilon_i(V) = \epsilon_i^0 + (z/L)V$, with L being the distance between the two electrodes attached to the S atoms and z the distance between the ith atom to the anode. We see from Fig. 11(a) that the applied voltage induces a change in excess charges of the two N atoms, which in turn gives rise to energy splittings among the t_{2g} orbitals, as shown in Fig. 11(b). Substituting the obtained E_i in Hamiltonian (2.1), we calculate the g-factor of the ground state and the magnetic susceptibility at room temperature as a function of the applied voltage and plot them in Figs. 11(c) and 11(d). The anisotropic g-factors can be tuned between 0 and over 3 under a voltage less than 1 V, and the magnetic susceptibility can be significantly increased or decreased by
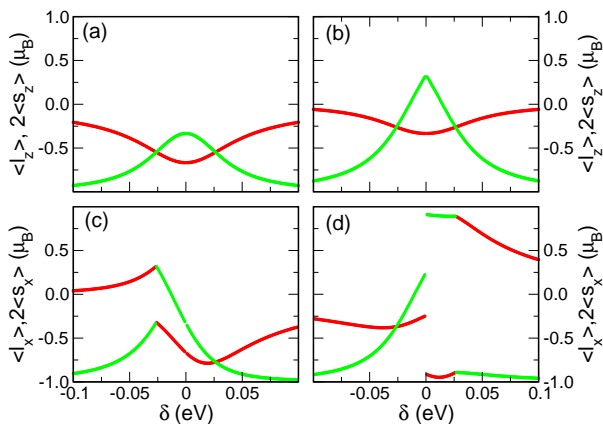
20

Figure 10: Magnetic-moment contributions from the orbital and spin angular momenta for the ground states (a) and (c) and for the first excited state (b) and (d). Red and green lines represent the orbital and spin respectively.

the electric voltage, depending on the magnetic-field direction. The tunability of g-factor in such a molecule is extraordinary in terms of both range and responsivity.

The electrically controlled g-factor and magnetism in conjugated metallorganic molecules will allow electron spin resonance with a spatial resolution at the molecular level under a homogeneous magnetic field, which is important to coherently manipulate individual electron spins, a prerequisite to quantum computations. In addition, by controlling the magnetic moment and susceptibility, quantum information in individual spins can be selectively exposed, hidden, or processed, which can be used for quantum encryption, smart memory, and other spin logic devices. The complete model of TMSAMs and the electrically controlled g-factor in TMSAMs were published in the paper, "Electrically controlled g-factor and magnetism in conjugated metallorganic molecules", *Phys. Rev. B* **78**, 212411 (2008).

7 Spatially correlated fluctuations of donor and acceptor in FRET

We have applied our knowledge on polarons gained in this study to understand the single-molecule fluorescent energy transfer (FRET) in polyproline. FRET is a powerful and convenient optical tool to track biological conformational changes. In FRET, a donor fluorophore is excited by incident light to create an exciton, which can transfer to an
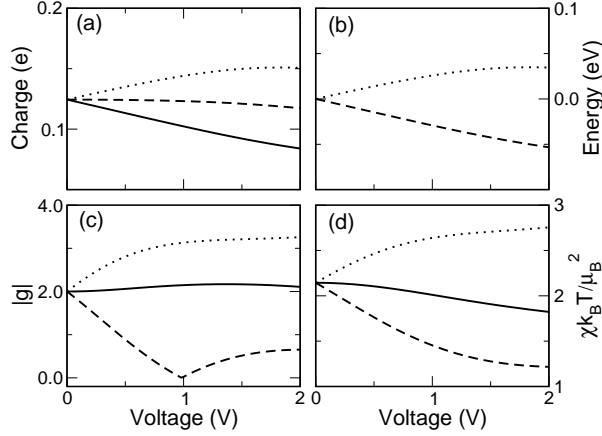
Figure 11: Voltage-dependent charge of the two N atoms in the ligand with the dithiol groups (a), energy E_i of the t_{2g} orbitals (b), $|g^\nu|$ of the ground state (c), and magnetic susceptibility χ^ν (d). Solid and dotted lines in panel (a) plot the charge on individual N atoms, and the dashed line is the average. Dotted and dashed lines in panel (b) plot the energies of d_{xz} and d_{yz}, respectively. The energy of d_{xy} is fixed at 0. Solid, dotted, and dashed lines in panel (c) and (d) are for $\nu = z$, x, and y, respectively.

acceptor in close proximity, leading to a reduction in the donor's fluorescence intensity and an increase in the acceptor's emission intensity. Förster showed several decades ago that the transfer rate k depends on the donor-acceptor distance r in a power law, $k \propto 1/r^6$, which is the scientific foundation of using FRET as a "spectroscopic ruler".

The Förster's theory assumes that motions of donors and acceptors are completely decoupled, i.e., $\langle x_1 x_2 \rangle = 0$ with x_i being the fluctuations in donor ($i = 1$) and accptor ($i = 2$). Recent advancement in the FRET technology makes it possible to detect biological activity at the single-molecule level. Fundamentally, as the size of a system reduces to such a microscopic level, the atomic motions become less stochastic but more coherent. Since a donor-acceptor pair in most single-molecule FRET measurements is connected through a common molecule, one expects that coherent atomic motions in the molecule would translate into an undiminished correlation between fluctuations of the donor and the acceptor.

We note that a donor and an acceptor in single-molecule FRET are attached to a same molecule, as shown in Fig. 12, or more generally, a common environment, which has low-energy excitations with a typical dispersion $\omega_{\boldsymbol{q}} \propto |\boldsymbol{q}|$, where $\boldsymbol{q}$ is the momentum and $\omega_{\boldsymbol{q}}$ the frequency. Consequently, the equilibrium position x_i^0 of the displacement x_i are slowly fluctuating. For a quasi one-dimensional (1d) long molecule, such as DNA and
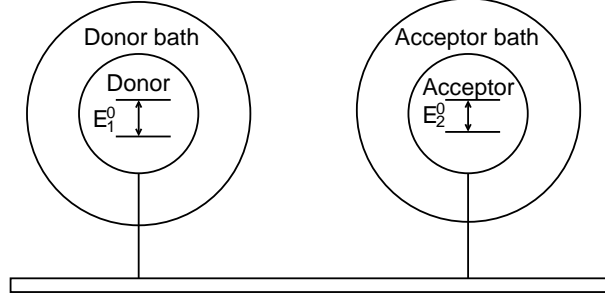
Figure 12: Schematic diagram showing the donor-acceptor correlation and its effect on the donor and acceptor baths. The donor and the acceptor are attached to a molecule, represented by the long bar, which mediates the interaction between the two baths, respresented by the two ring areas.

polyproline, where acoustic phonons are the main low-energy excitations,

$$\overline{x_1^0 x_2^0} \propto \sum_{|q| \geq \xi^{-1}} \frac{1}{NM\beta\omega_q^2} e^{iqR} \propto \int dq \frac{e^{iqR}}{\beta(q^2 + \xi^{-2})} \propto \frac{e^{-R/\xi}}{\beta},$$

where $\beta \equiv 1/k_B T$ with k_B being the Boltzmann constant and T temperature, $R = |R_1 - R_2|$ is the molecular contour length between donor and acceptor, and $\beta\hbar\omega_q \ll 1$ has been used. Here we have introduced a low-momentum cut-off ξ^{-1}, which is due to the finite length of a molecule. For a flexible molecule, ξ is determined by a persistence length beyond which the bending become significant. Defining Γ as the correlation strength, we can write

$$\overline{x_1^0 x_2^0} = \frac{\Gamma}{\beta} e^{-R/\xi}. \tag{7.1}$$

Hence a correlation between the donor and acceptor fluctuations entails an effective coupling between the two baths, $\langle Q_{1\lambda} Q_{2\lambda} \rangle \neq 0$, where $Q_{i\lambda}$ are normal coordinates in bath i.

To describe the interacting baths, we augment the noninteracting H_b^0, which can be written in terms of normal coordinates, $H_b^0 = \frac{1}{2} \sum_{i\lambda} (P_{i\lambda}^2 + \omega_\lambda^2 Q_{i\lambda}^2)$, by a crossing term

$$H_b = H_b^0 - \sum_\lambda \gamma_\lambda \omega_\lambda^2 Q_{1\lambda} Q_{2\lambda}. \tag{7.2}$$

Under this new Hamiltonian of the baths, $\langle Q_{1\lambda} Q_{2\lambda} \rangle$ can be evaluated via

$$\langle Q_{1\lambda} Q_{2\lambda} \rangle = \int dQ_{1\lambda} dQ_{2\lambda} Q_{1\lambda} Q_{2\lambda} e^{-\beta H_b} = \frac{\gamma_\lambda}{\beta\omega_\lambda^2(1 - \gamma_\lambda^2)}.$$

23

If we assume that γ_λ is independent of λ, $\gamma_\lambda = \gamma$, we obtain, from Eqs. (6) and (7),

$$\frac{\gamma}{1-\gamma^2} = \frac{\Gamma}{\eta}e^{-R/\xi}, \tag{7.3}$$

where $\eta \equiv \int_0^\infty d\omega J(\omega)/\omega$ is the reorganization energy. For the widely used Debye spectral density, $J_{\mathrm{De}}(\omega) = \frac{\eta_0\omega_c\omega}{\omega^2+\omega_c^2}$, $\eta = \eta_0$. The positive definitiveness of H_b requires $\gamma < 1$. Equation (7.3) relates the coupling between two baths to the correlation function in a molecule that connects them.

We derive the rate of energy transfer in the presence of the spatial correlation,

$$k \propto \sqrt{\frac{\beta(1+\gamma)}{\eta}} \exp\left\{-\frac{\beta[(1+\gamma)\Delta - \eta]^2}{4\eta(1+\gamma)}\right\}\frac{1}{r^6}, \tag{7.4}$$

which extends the original Förster's theory. If we write the transfer rate at $\gamma = 0$ as $k_0 = \tau_D^{-1}(r_0/r)^6$ with τ_D being the donor fluorescent lifetime in the absence of an acceptor, the transfer rate of Eq. (7.4) is $k = \Lambda(R)k_0$, where

$$\Lambda(R) = (1+\gamma)^{\frac{1}{2}} \exp\left\{-\beta\frac{\gamma}{4(1+\gamma)\eta}\left[(1+\gamma)\Delta^2 - \eta^2\right]\right\}. \tag{7.5}$$

Consequently the fluorescent transfer efficiency, $E \equiv 1-\tau_D'/\tau_D$ (τ_D' is the donor fluorescent lifetimes in the presence an acceptor), as a function of R is

$$E(R) = \left[1 + \Lambda^{-1}(R)\left(\frac{r}{r_0}\right)^6\right]^{-1}. \tag{7.6}$$

It is readily seen that when $\gamma = 0$, $\Lambda = 1$ and the above expression reduces to the Förster formula, $E = [1 + (r/r_0)^6]^{-1}$. In the case of weak correlations, where $\gamma \ll 1$, $\Lambda \propto \exp[-\beta\gamma(\Delta^2 - \eta^2)/4\eta]$, and we see that nonzero γ would *reduce* the transfer rate. This can be understood by noticing that the transfer is facilitated only by the out-of-phase modes, which have higher frequencies because of the couplings between the baths and are therefore more difficult to be excited. Figure 13 illustrates effects of the donor-acceptor correlation on the exciton transfer rate k and efficiency E in a system with representative parameters, $\Delta = 0.45$ eV, $\eta = 0.1$ eV, and $r_0 = 5.4$ nm (see below). It is also temporarily set $R = r$, i.e, the molecule is rigid. We see that at short distances, the transfer rate is reduced in the presence of the donor-acceptor correlation, compared to that from the Förster formula. This reduction decreases with the donor-acceptor distance and eventually diminishes when the distance is greater than ξ. From the transfer-efficiency plot in the
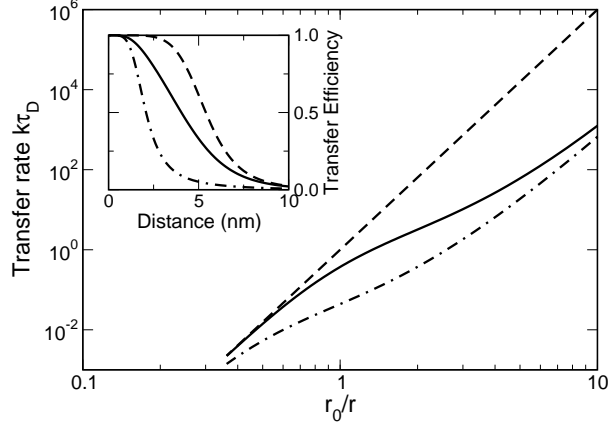
Figure 13: Transfer rate $k\tau_D$ as a function of distance for different correlation lengths ξ. Dashed, solid, and dot-dashed lines correspond to $\xi = 0$ (no correlation), 2.4, 5 nm, respectively. The inset shows the transfer efficiency E as a function of r. Other parameters are $\Gamma = 0.05$ eV, $\Delta = 0.45$ eV, $\eta = 0.1$ eV, and $r_0 = 5.4$ nm.
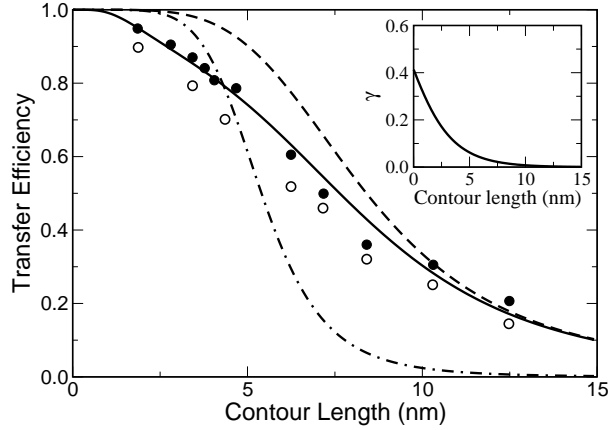
Figure 14: Transfer efficiency E as a function of the contour length. Filled and open circles are the mean transfer efficiencies from SMM and TCSPM, respectively. The lines are theoretical results from Eq. (21) with three parameter sets: (1) $\Gamma = 0.05$ eV and $\xi = l_0 = 2.4$ nm (solid); (2) $\Gamma = 0$ and $l_0 = 2.4$ nm (dashed); (3) $\Gamma = 0$ and $l_0 = \infty$ (dot-dashed). The inset shows γ as a function of the contour length. Other parameters are as in Fig. 2.

25

inset of Fig. 13, we see that the donor-acceptor correlation leads to a smaller effective Förster radius.

We apply the theory to a recent systematic single-molecule FRET study of 1d polyproline. Such a long molecule is susceptible to bending. The straight-line distance r between two points with contour length R in the chain can be written as

$$\langle r^2 \rangle = 2\alpha^2 \beta^2 \Big(\frac{R}{\alpha\beta} - 1 + e^{-\frac{R}{\alpha\beta}} \Big), \tag{7.7}$$

where $2\alpha^{-1} = \alpha_1^{-1} + \alpha_2^{-1}$. From Eq. (7.6), we have

$$E(R) = \Big[1 + 8\Lambda^{-1}(R) \Big(\frac{l_0}{r_0} \Big)^6 \Big(\frac{R}{l_0} + e^{-\frac{R}{l_0}} - 1 \Big)^3 \Big]^{-1}. \tag{7.8}$$

where $l_0 \equiv \alpha\beta$ defines the persistence length of a flexible molecule. An excellent fit is found, as shown by the solid line in Fig. 14 for the entire experimentally measured range of R, by using $\Gamma = 0.05$ eV and $\xi = 2.4$ nm. If both Γ and ξ are set zero, namely, the donor-acceptor correlation is absent and the molecule is rigid, the transfer rate reduces to the well-known Förster result, as shown by the dot-dashed line in Fig. 14, which, compared to the experimental data, overestimates the transfer efficiency at shorter contour lengths (< 5 nm) and underestimates the efficiency at longer contour lengths (> 5 nm). If we neglect the correlation but allow the molecule to bend, the transfer rate is in a fairly good agreement with experiment for contour lengths larger than 10 nm, but seriously overestimates the rate at shorter contour lengths, suggesting that the donor-acceptor correlation is particularly important at short contour lengths, where the molecular bending is weak. The strong correlation effect at short distances is also reflected in the γ versus R plot, as shown in the inset of Fig. 14, where $\gamma \geq 0.2$ for $R \leq 2.0$ nm, suggesting that the donor and acceptor baths are strongly coupled at those distances.

The complete theory that describes the correlated fluctuations in the donor and acceptor and their effect on FRET and its application to polyproline were published in the paper, "Fluorescent resonant energy transfer: Correlated fluctuations of donor and acceptor", *J. Chem. Phys.* **127**, 221101 (Communications) (2007). This theory complements the original Förster theory, where motions of donor and acceptor are completely uncorrelated. Because of the theorys simplicity and importance, our paper, was the 3rd most downloaded papers of the journal in December of 2007.

26

8 Electrical transport and noninvasive detection of spins in N@C$_{60}$ and TMSAMs

The electron spin at the central N atom in endohedral N@C$_{60}$ or at the transition-metal ion in a TMSAM has a very long electron spin relaxation time, showing its great potential in quantum information storage and processing. For applications in the fields of quantum information and spintronics, it is desired that dynamics of individual spins rather than an ensemble average of spins be measured and recorded, which requires a highly sensitive probe of electron spin resonance (ESR) and more generally spin dynamics. ESR, which is commonly measured from microwave absorption, can also be detected electrically by observing the change in the conductivity of the system and electrically detected ESR (EDESR) has been extensively used in studies of defects in semiconductors with sensitivity often higher than conventional ESR detection by several orders of magnitude. In N@C$_{60}$ and TMSAMs, because of the intimate coupling between the central spin and delocalized π electrons in the conjugated C$_{60}$ and ligands, as well as the high conductance of π-conjugated C$_{60}$ and ligands, we expect that a much higher sensitivity in EDESR, possibly to a single molecule resolution, can be achieved in N@C$_{60}$ and TMSAM. This electrical detection of spin dynamics is noninvasive in that an injected electron into N@C$_{60}$ or a TMSAM would traverse along the π-conjugated pathways without spoiling the central spin at the N atom or at the transition-metal ion. This is in contrast to quantum dots and related structures where an injected electron into a system with an electron spin would destroy the original spin (invasive), resulting in loss of quantum information contained in that spin.

8.1 Device structure and Hamiltonian

We consider a device structure (shown in Fig. 15), where an N@C$_{60}$ molecule is placed between two metallic electrodes. A scanning tunneling microscope (STM) tip can also serve as an electrode. A DC magnetic field $\boldsymbol{H}_0$ is along the z axis, $\boldsymbol{H}_0 = H_0 \boldsymbol{e}_z$, and the microwave magnetic $\boldsymbol{H}_1$ is in the x-y plane. The proposed device structure is experimentally feasible since all essential components have been successfully demonstrated.

The Hamiltonian of the system comprises four parts,

$$H = H_\alpha + H_{\alpha'} + H_{\text{N@C}_{60}} + H_{\text{C}}. \tag{8.1}$$

Here $H_{\alpha(\alpha')}$ describes the left (right) electrode, which is assumed to be a conventional metal or ferromagnet, with a Fermi energy $\mu_{\alpha(\alpha')}$ and a spin-polarised density of states, $\rho_{\alpha(\alpha')}(\omega) = \rho_{\alpha(\alpha')\uparrow}(\omega) + \rho_{\alpha(\alpha')\downarrow}(\omega)$, where ω is the energy. $H_{\text{N@C}_{60}}$ represents an isolated

endohedral N@C$_{60}$ molecule, $H_{\text{N@C}_{60}} = H_{\text{C}_{60}} + H_{\text{ex}}$, where $H_{\text{C}_{60}}$ is the Hamiltonian of a C$_{60}$ molecule,

$$H_{\text{C}_{60}} = -\sum_{\langle ij \rangle \sigma} [t_0 - \alpha_0(d_{ij} - d_0)](c_{i\sigma}^\dagger c_{j\sigma} + \text{H.c.}) + \sum_{i\sigma} \epsilon_i(V) c_{i\sigma}^\dagger c_{i\sigma} + \frac{1}{2}K \sum_{\langle ij \rangle} (d_{ij} - d_0)^2. \quad (8.2)$$

and H_{ex} is the exchange interaction between electrons in C$_{60}$ and the central spin $\boldsymbol{S}$ at the N atom,

$$H_{\text{ex}} = J \sum_{i\sigma\sigma'} c_{i\sigma}^\dagger \hat{\boldsymbol{\sigma}}_{\sigma\sigma'} c_{i\sigma'} \cdot \boldsymbol{S}. \quad (8.3)$$

Here we use a tight-binding π-electron model for C$_{60}$, which resembles the Su-Schrieffer-Heeger (SSH) model for π-conjugated polymers. $c_{i\sigma}^\dagger$ creates a π electron at site i with spin σ ($\uparrow$ or $\downarrow$) along the spin quantization axis $\boldsymbol{e}_z$, i.e., the direction of $\boldsymbol{H}_0$), α_0 is the electron-lattice coupling, d_{ij} is the bond length between the adjacent ith and jth atoms and K is the elastic constant for C-C σ bonds. ϵ_i is the electron energy at site i, which is a function of an applied voltage V. The coupling between the spin at the central N atom, $\boldsymbol{S}$, and π electrons in the C$_{60}$ cage is through an exchange interaction, which originates from the overlap between electron wave functions of the N atom and of the C$_{60}$, and $\hat{\boldsymbol{\sigma}}$ are Pauli matrices. The exchange strength is about $J = 10^{-4}$ eV. H_{C} is the coupling between the electrodes and N@C$_{60}$, and it is assumed that only the four atoms that are closest to the electrodes have a direct electronic coupling to the electrodes,

$$H_C = \sum_{\sigma\sigma', a=\{1,5\}} [T_{\sigma\sigma'} c_{\alpha\sigma'}^\dagger c_{a\sigma} + T_{\sigma'\sigma}^* c_{a\sigma}^\dagger c_{\alpha\sigma'}] + \sum_{\sigma\sigma', b=\{51,56\}} [T'_{\sigma\sigma'} c_{\alpha'\sigma'}^\dagger c_{b\sigma} + T'^*_{\sigma'\sigma} c_{b\sigma}^\dagger c_{\alpha'\sigma'}], \quad (8.4)$$

where $c_{\alpha\sigma}^\dagger$ ($c_{\alpha'\sigma}^\dagger$) creates an electron with spin σ in the left (right) electrode along the electrode magnetization, $\boldsymbol{m}_{L(R)}$, and $T_{\sigma\sigma'}$ ($T'_{\sigma\sigma'}$) is the electron hopping matrix element from spin σ in the C$_{60}$ to the spin σ' in the left (right) electrode, which depends on the relative orientation between $\boldsymbol{e}_z$ and $\boldsymbol{m}_{L(R)}$. One possible model for T and T' is that the spin dependence is due purely to an $SU(2)$ spin rotation

$$T = t \begin{pmatrix} \cos\frac{\theta_L}{2} e^{i\phi_L/2} & \sin\frac{\theta_L}{2} e^{i\phi_L/2} \\ -\sin\frac{\theta_L}{2} e^{-i\phi_L/2} & \cos\frac{\theta_L}{2} e^{-i\phi_L/2} \end{pmatrix}, \quad T' = t' \begin{pmatrix} \cos\frac{\theta_R}{2} e^{i\phi_R/2} & \sin\frac{\theta_R}{2} e^{i\phi_R/2} \\ -\sin\frac{\theta_R}{2} e^{-i\phi_R/2} & \cos\frac{\theta_R}{2} e^{-i\phi_R/2} \end{pmatrix},$$

where $\boldsymbol{m}_{L(R)} = (\sin\theta_{L(R)} \cos\phi_{L(R)}, \sin\theta_{L(R)} \sin\phi_{L(R)}, \cos\theta_{L(R)})^T$, t and t' are the magnitudes of hopping integral. These hopping matrices exclude spin-flip hopping between the electrode and the molecule. When the spin-flip hopping is not entirely forbidden, due, for

example, to the spin-orbit coupling in the electrode, $T_{\sigma\sigma'}$ ($T'_{\sigma\sigma'}$) should be augmented by $\delta T_{\sigma\sigma'}$ ($\delta T'_{\sigma\sigma'}$),

$$\delta T = t \begin{pmatrix} -\lambda^* \sin\frac{\theta_L}{2} e^{i\phi_L/2} & \lambda\cos\frac{\theta_L}{2} e^{-i\phi_L/2} \\ \lambda^*\cos\frac{\theta_L}{2} e^{i\phi_L/2} & \lambda\sin\frac{\theta_L}{2} e^{-i\phi_L/2} \end{pmatrix}, \; \delta T' = t' \begin{pmatrix} -\lambda^* \sin\frac{\theta_R}{2} e^{i\phi_R/2} & \lambda\cos\frac{\theta_R}{2} e^{-i\phi_R/2} \\ \lambda^*\cos\frac{\theta_R}{2} e^{i\phi_R/2} & \lambda\sin\frac{\theta_R}{2} e^{-i\phi_R/2} \end{pmatrix},$$

where $\lambda \equiv \lambda_1 + i\lambda_2$ characterizes the relative importance of spin-flip hopping with respect to spin-conserve hopping, and $|\lambda|$ in general is much less than 1.

8.2 Keldysh non-equilibrium Green's function formalism

In detection of coherent spin dynamics, it is important to retain the phase information. To this end, we use the Keldysh non-equilibrium Green's functions to evaluate the current across the electrode/N@C$_{60}$/electrode configuration. The current flowing out the left electrode is

$$I_L = -e\langle \dot{N}_L \rangle = \frac{-ie}{\hbar}\langle [H, N_L] \rangle = \frac{e}{\hbar}\sum_{\sigma\sigma'}\int_{-\infty}^{+\infty}\frac{d\omega}{2\pi}[T_{\sigma\sigma'}G^+_{a\sigma,\alpha\sigma'}(\omega) - T^*_{\sigma'\sigma}G^+_{\alpha\sigma',a\sigma}(\omega)] \quad (8.5)$$

where $N_L = \sum_{\alpha\sigma} c^\dagger_{\alpha\sigma}c_{\alpha\sigma}$. The Green's functions G^+ in the time domain are defined as $G^+_{ij}(t,t') \equiv i\langle c^\dagger_j(t')c_i(t)\rangle$ and $G^-_{ij}(t,t') \equiv -i\langle c_i(t)c^\dagger_j(t')\rangle$. Using the Dyson equations for the non-equilibrium Green's functions, we obtain that for a device under an applied voltage $V = (\mu_{\alpha'} - \mu_\alpha)/e$,

$$I_L = \int_{\mu_L}^{\mu_L+eV}\frac{d\omega}{2\pi}g(\omega,V) \equiv \int_{\mu_L}^{\mu_L+eV}\frac{d\omega}{2\pi}\sum_{a=\{1,6\},b=\{51,56\}}\sum_{\eta\eta'}\frac{e}{\hbar}C_{\eta\eta'}A_{\eta'\eta} \quad (8.6)$$

where $g(\omega,V)$ is the conductance and

$$C_{\eta\eta'} = T_{\eta\uparrow}\rho_{\alpha\uparrow}(\omega)T_{\uparrow\eta'} + T_{\eta\downarrow}\rho_{\alpha\downarrow}(\omega)T_{\downarrow\eta'},$$

$$A_{\eta'\eta} = \sum_{\sigma\sigma'}G^r_{a\eta',b\sigma}(\omega)[T'_{\sigma\uparrow}\rho_{\alpha'\uparrow}(\omega)T'_{\uparrow\sigma'} + T'_{\sigma\downarrow}\rho_{\alpha'\downarrow}T'_{\downarrow\sigma'}]G^a_{b\sigma',a\eta}(\omega),$$

where the advanced and retarded Green's functions in the time domain defined as $G^a_{ij}(t,t') \equiv i\theta(t'-t)\langle\{c_i(t),c^\dagger_j(t')\}\rangle$ and $G^r_{ij}(t,t') \equiv -i\theta(t-t')\langle\{c_i(t),c^\dagger_j(t')\}\rangle$, where $\theta(x)$ is the Heaviside step function and $\{,\}$ is the anticommutator.

Equation (8.6) expresses the device conductance in terms of the Green's function of N@C$_{60}$, $G^{r(a)}_{a\sigma,b\sigma'}$. Note that the Green's function $G^{r(a)}_{a\sigma,b\sigma'}$ is the full Green's function with the effect of the electrodes contained in its self energy. Consequently, both sequential tunneling and co-tunneling processes are included in Eq. (8.6).
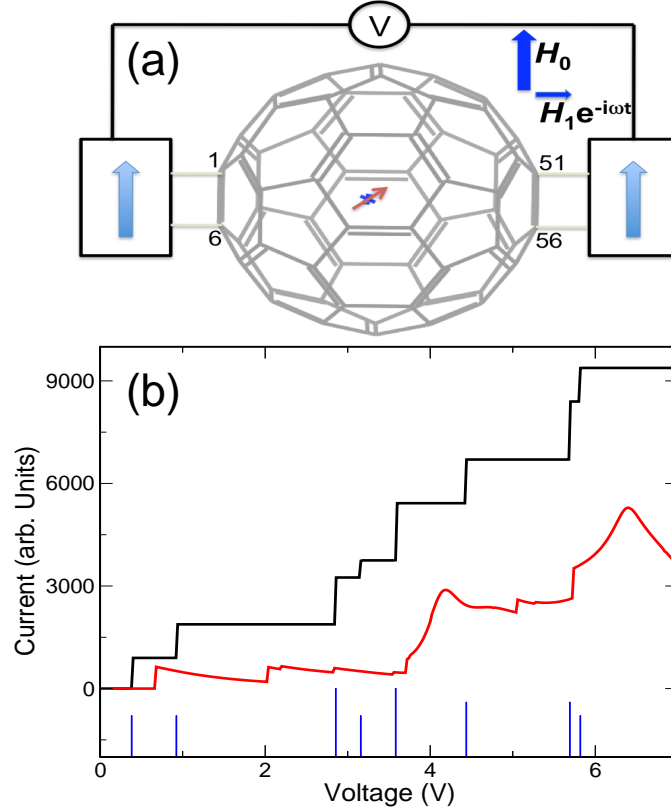
Figure 15: (a) Schematic diagram of electrical detection of electron spin dynamics in the ferromagnet/N@C_{60}/ferromagnetic structure. The central N atom inside the C_{60} cage has an electron spin $S = 3/2$. Electrons flow in C_{60} from the magnetic electrodes via the four C atoms (1, 6, 51, and 56). The static and microwave magnetic fields, $\boldsymbol{H}_0$ and $\boldsymbol{H}_1$, are used to change spin dynamics. An electrical gate (not shown) can be included to modify the charge state of N@C_{60}. (b) I-V characteristics of the device structure in equilibrium ($H_1 = 0$). The black line describes the case where the site energy in a neutral C_{60} is independent of voltage, and the red line describes the case where the site energy change is proportional to the voltage. The blue bars indicate the energy levels of a neutral C_{60}, and the bar height represents the energy degeneracy.

8.3 Green's functions of N@C$_{60}$

Since the exchange energy between the central spin and C$_{60}$ electrons, $J = 10^{-4}$ eV, is very small compared to any energy scales in $H_{C_{60}}$, it does not affect the geometry of the C$_{60}$, which can be obtained by minimizing the total energy E_t (summation of π-electron energies and elastic energy from σ bonds) of the single-electron Hamiltonian $H_{C_{60}}$, $\partial E_t/\partial d_{ij} = 0$. With the optimized geometry $H_{N@C_{60}}$ can be written as

$$H_{N@C_{60}} = \sum_{m\sigma} \epsilon_m c_{m\sigma}^\dagger c_{m\sigma} + \sum_{m\sigma\sigma'} J_m c_{m\sigma}^\dagger \hat{\boldsymbol{\sigma}}_{\sigma\sigma'} c_{m\sigma'} \cdot \hat{\boldsymbol{S}}. \tag{8.7}$$

where ϵ_m is eigen energy of the mth eigen state, ψ_m, $c_m^\dagger$ creates an electron at the mth eigenstate, and $J_m = \sum_i \langle i|\psi_m\rangle\langle\psi_m|i\rangle = J$ is the exchange coupling between the mth eigen state and $\boldsymbol{S}$. To the leading term of J, the eigen energy of each level is

$$\lambda_{m\pm} = \epsilon_m \pm J_m|\langle\hat{\boldsymbol{S}}\rangle| \equiv \epsilon_m \pm J_m S, \tag{8.8}$$

where $S = \sqrt{S_x^2 + S_y^2 + S_z^2}$ with $S_q = \langle\hat{S}_q\rangle$ $(q = x, y, z)$, and $\pm$ represents up- and down-spin state along the direction of the averaged $\langle\hat{\boldsymbol{S}}\rangle$. The Green's function in the spin space is a 2×2 matrix, which can be written as a summation of a scalar and a vector,

$$\hat{G}_{ij}(\omega) = \begin{pmatrix} G_{i\uparrow j\uparrow} & G_{i\uparrow j\downarrow} \\ G_{i\downarrow j\uparrow} & G_{i\downarrow j\downarrow} \end{pmatrix} \equiv \overline{G}_{ij}^{r(a)}(\omega)\hat{1} + \boldsymbol{G}_{ij}^{r(a)}(\omega) \cdot \hat{\boldsymbol{\sigma}}. \tag{8.9}$$

$$\overline{G}_{ij}^r(\omega) = \sum_m \frac{(\omega - \epsilon_m)\langle i|\psi_m\rangle\langle\psi_m|j\rangle}{(\omega - \lambda_{m+} + i\Gamma/2)(\omega - \lambda_{m-} + i\Gamma/2)},$$

$$\boldsymbol{G}_{ij}^r(\omega) = \sum_m \frac{J_m \boldsymbol{S}\langle i|\psi_m\rangle\langle\psi_m|j\rangle}{(\omega - \lambda_{m+} + i\Gamma/2)(\omega - \lambda_{m-} + i\Gamma/2)} \equiv g_{ij}^r \boldsymbol{S}.$$

$\hat{G}_{ij}^a$ can be obtained by replacing Γ by $-\Gamma$ in $\hat{G}_{ij}^r$. We see that the Green's function between any two sites in the C$_{60}$ molecule depends on the central spin $\boldsymbol{S}$ in a transparent manner.

For detection of spin dynamics, a quick electrical response to spin dynamics is necessary. Thus we focus our attention in this paper on the non-resonant co-tunneling regime at a low voltage, where the current is controlled by conductance $g(\mu_\alpha = \mu_{\alpha'} = \mu, V = 0)$. At the Fermi level, the density of states for the electrodes can be approximately written as $\rho_{\alpha\uparrow(\downarrow)}(\mu) = \rho_\alpha(\mu)[1 + (-)p_\alpha]/2$ and $\rho_{\alpha'\uparrow(\downarrow)}(\mu) = \rho_{\alpha'}(\mu)[1 + (-)p_{\alpha'}]/2$, where $p_{\alpha(\alpha')}$ is the spin polarization of the conductivity in the electrode. If spin-flip hopping at the contacts

31

is forbidden, i.e., $\lambda = 0$ in T and T', and the magnetizations of the two electrodes are parallel to the quantization axis, we have

$$g(\mu, 0) \propto \sum_{ab}[(1+p_\alpha p_{\alpha'})(|\overline{G}_{ab}^r|^2 + |g_{ab}^r|^2 S_z^2) + 2(p_\alpha + p_{\alpha'})\overline{G}_{ab}^r g_{ab}^a S_z + (p_\alpha - p_{\alpha'})|g_{ab}^r|^2 (S_x^2 + S_y^2)].$$
(8.10)

According to Eq. (8.10), the electrical detection is much more sensitive to the longitudinal spin component than the transverse one. Furthermore, that linear term is proportional to the total spin polarization of the two electrodes, $p_\alpha + p_{\alpha'}$, suggesting that ferromagnetic electrodes would greatly enhance the spin signals in electrical transport compared to nonmagnetic electrodes that are used in most EDESR experiments.

If the spin-flip hopping is partially allowed, the conductance

$$g_{sf}(\mu, 0) \propto \sum_{ab}[2g_{ab}^r \overline{G}_{ab}^a (\lambda_1 S_x - \lambda_2 S_y) + (p_\alpha + p_{\alpha'})|g_{ab}^r|^2 (\lambda_1 S_x - \lambda_2 S_y)S_z]. \qquad (8.11)$$

We see that the real (λ_1) and imaginary (λ_2) parts of the spin-flip hopping exposes the transverse components S_x and S_y to the electrical transport. We see that the real (λ_1) and imaginary (λ_2) parts of the spin-flip hopping exposes the transverse components S_x and S_y to the electrical transport.

8.4   Spin dynamics and its signatures in transport

The spin dynamics, including resonance, precession, and relaxation, can be described by the Bloch equation,

$$\frac{d\boldsymbol{S}}{dt} = \gamma \boldsymbol{S} \times \boldsymbol{H} - \frac{S_x \boldsymbol{e}_x + S_y \boldsymbol{e}_y}{T_2} - \frac{S_z - S_0}{T_1}\boldsymbol{e}_z. \qquad (8.12)$$

The Bloch equation is valid for both an individual spin and an ensemble average of spins (magnetization). Here $\gamma = g_N \mu_B / \hbar$ is the magnetogyric ratio with g_N being the g-factor for the electron spin in N@C$_{60}$, which is 2, identical to that for a free electron, and μ_B the Bohr magneton. $\boldsymbol{H}$ is the total applied magnetic field, consisting of a DC field $\boldsymbol{H}_0$ along the z-axis and a circularly polarised microwave field with a frequency ω in the neighborhood of the resonance frequency $\omega_0 = \gamma H_0$, $\boldsymbol{H}_1 = H_1(\boldsymbol{e}_x \cos \omega t + \boldsymbol{e}_y \sin \omega t)$. S_0 is the equilibrium value of the spin, and T_1 and T_2 are the longitudinal and transverse spin relaxation times.

The Bloch equation is analytically solvable, and the general solution of $\boldsymbol{S}$ can be written as $q = (x, y, z)$,

$$S_q = C_1 e^{-\zeta\tau} + C_2 e^{-\xi\tau} \cos \eta\tau + \frac{C_3}{\eta} e^{-\xi\tau} \sin \eta\tau + C_4, \qquad (8.13)$$
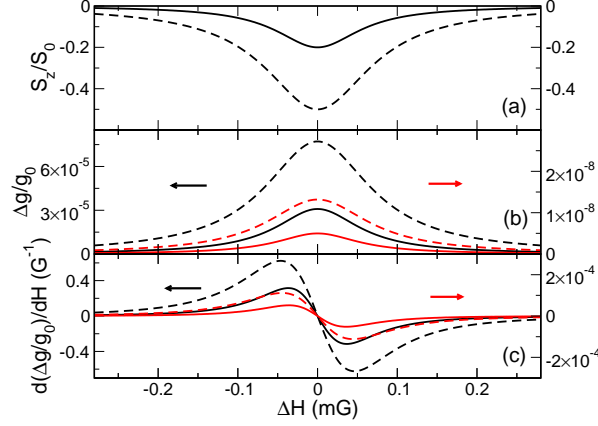
Figure 16: Electrically detected electron spin resonance in N@C_{60} when slowly sweeping the DC magnetic field $\boldsymbol{H}_0 = H_0\boldsymbol{e}_z$ under a fixed microwave frequency ω. Panels (a), (b) and (c) describe the longitudinal spin component S_z, relative conductance change $\Delta g/g_0$, and derivative $d(\Delta g/g_0)/dH_0$ as a function of $\Delta H = H_0 - \omega/\gamma$. Solid and dashed lines correspond to $H_1 = 1/2\gamma\sqrt{T_1 T_2}$ and $1/\gamma\sqrt{T_1 T_2}$, respectively. Black (red or gray) lines are for ferromagnetic electrodes $p_\alpha = p_{\alpha'} = 0.5$ (nonmagnetic electrodes $p_\alpha = p_{\alpha'} = 10^{-4}$). The parameters are $T_1 = 2T_2 = 2$ ms, $\gamma = 1.76 \times 10^7$ s^{-1}G^{-1}, $\omega = 5.28 \times 10^{10}$ s^{-1}, $S_0 = 0.25$, $\Gamma = 2 \times 10^{-5}$ eV, and $J = 10^{-4}$ eV.

where $\tau = \gamma H_1 t$, and the eigen values ζ and $\xi \pm i\eta$ are the three roots of the cubic equation, $(x + \phi)(x + \eta)^2 + x + \eta + \kappa^2(x + \phi) = 0$, where $\phi = 1/\gamma H_1 T_1$, $\eta = 1/\gamma H_1 T_2$, and $\kappa = (\omega_0 - \omega)/\gamma H_0$. The coefficients C_i ($i = 1, ..., 4$) are determined by the initial conditions and asymptotic behavior at $t = \infty$.

The Bloch equation has a steady-state solution, where S_x and S_y precess around $\boldsymbol{H}_0$ at frequency ω and S_z remains constant. In most EDESR experiments, the microwave frequency ω is xed and the DC magnetic eld H_0 is swept to meet the resonance condition. Figure 16 shows the calculated conductance change, $\Delta g = g(\mu, 0) - g_0$, with g_0 being $g(\mu, 0)$ in the absence of the microwave $\boldsymbol{H}_1$, as a function of $\Delta H = \omega/\gamma - H_0$. S_0 is fixed at $S_0 = 0.25$. The conductance reaches maximum at the resonance, and its dependence of ΔH is a mirror image of that of S_z. The relative conductance change of $\Delta g/g_0 \sim 10^{-4}$ is remarkable, for EDESR can routinely detect the relative current change of 10^{-9}. The derivative plot, $d\Delta g/dH$ versus H, also shown in Fig. 16, is widely used to pinpoint the magnetic field H_0 at which the spin resonance occurs $[(d\Delta g/dH)_{H_0} = 0]$, and the material g-factor can be obtained from $g_N = \omega/\mu_B H_0$. We also compare the signals between ferromagnetic and nonmagnetic electrodes in Fig. 16. For a small $p_\alpha = 10^{-4}$, a
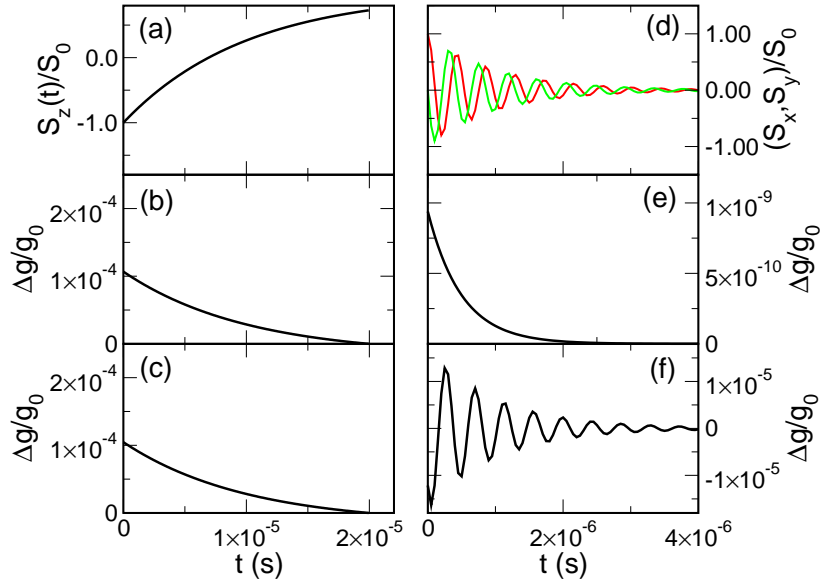
33

Figure 17: Transient relative conductance change due to longitudinal and transverse spin relaxation in N@C$_{60}$. Panel (a) describes the free relaxation of S_z after a π-pulse, and panels (b) and (c) plot the corresponding evolution of $\Delta g/g_0$ with spin-flip hopping forbidden ($\lambda = 0$) and spin-flip hopping allowed ($\lambda_1 = \lambda_2 = 0.05$), respectively. Panels (d) describes the damped precession of transverse spin components, S_x (red line) and S_y (green line) after a $\pi/2$-pulse followed by an on-resonance microwave $\boldsymbol{H}_1 = H_1(\cos \omega_0 t \boldsymbol{e}_x + \sin \omega_0 t \boldsymbol{e}_y)$. Panels (e) and (f) plot the corresponding $\Delta g/g_0$ as a function of time with $\lambda = 0$ and $\lambda_1 = \lambda_2 = 0.05$, respectively. $T_1 = 10 T_2 = 10^{-5}$ s. Other parameters are the same as in Fig. 16.

typical value for nonmagnetic electrodes, the signals are four orders of magnitude smaller than those with $p_\alpha = 0.5$, a typical value for magnetic electrodes.

We also study the transient response in conductance after short microwave pulses. The transient response in conductance can be used to measure T_1 and T_2. To measure T_1, we can apply a π-pulse at $t = 0$, and then turn off H_1 and monitor the conductance change. To measure T_2 we can follow a $\pi/2$ pulse with a large H_1 at the resonance frequency. The corresponding transient signals are displayed in Fig. 17.

An alternative and more appealing way to measure T_2 is to use transient nutation, which employs a large H_1 with $\gamma H_1 \gg 1/T_2$. Under this condition, the spin precesses around H_1 in the rotating frame, which makes S_z subject to both longitudinal and transverse spin relaxation. The initial condition before the application of H_1 is $\tilde{S}_x = \tilde{S}_y = 0$ and $S_z = S_0$, at resonance ($\kappa = 0$), from the general solution,

$$S_z \simeq S_0 \exp\left[-\frac{1}{2}\left(\frac{1}{T_1} + \frac{1}{T_2}\right)t \right]\left(\cos\tau + \frac{\eta - \phi}{2}\sin\tau\right), \tag{8.14}$$

we see that S_z decays with a time constant $2(T_1^{-1} + T_2^{-1})^{-1}$, which is $1/2T_2$ when $T_2 \ll T_1$ and T_2 if $T_2 = T_1$. Thus the transient nutation allows a sensitive measurement of T_2 in the conductance change. We solve the Bloch equation for different microwave frequency ω and calculate the conductance change as a function of ω and t, which is displayed in the color map of Fig. 18. We see that the change in conductance exhibits a damped oscillation. The oscillation is most pronounced near the resonance $\Delta\omega T_2 \leq 1$ and becomes diminished when away from the resonance. The time constant for the envelope function both on- and off-resonance is comparable to T_2. This color map resembles that in measured EDESR in C_{60}, and its features survive when the spin-flip hopping is allowed, as shown in the figure. The small splitting in the conductance peak around $\Delta\omega T_2 = 0$ can be used to estimate the relative importance of the spin-flip hopping.

The complete theory on spin-dependent transport across N@C_{60} and TMSAMs and its dependence on the dynamics of the central spin were contained in the manuscript, "Noninvasive electrical detection of electron spin dynamics at the N atom in N@C_{60}", which has been accepted by J. Phys: Condens. Matter.

9 Transfer lengths and spin injection from a 3d ferromagnet into graphene

Recent demonstration of large spin injection from a ferromagnetic electrode into graphene, together with graphene's outstanding transport attributes, suggest a promising potential
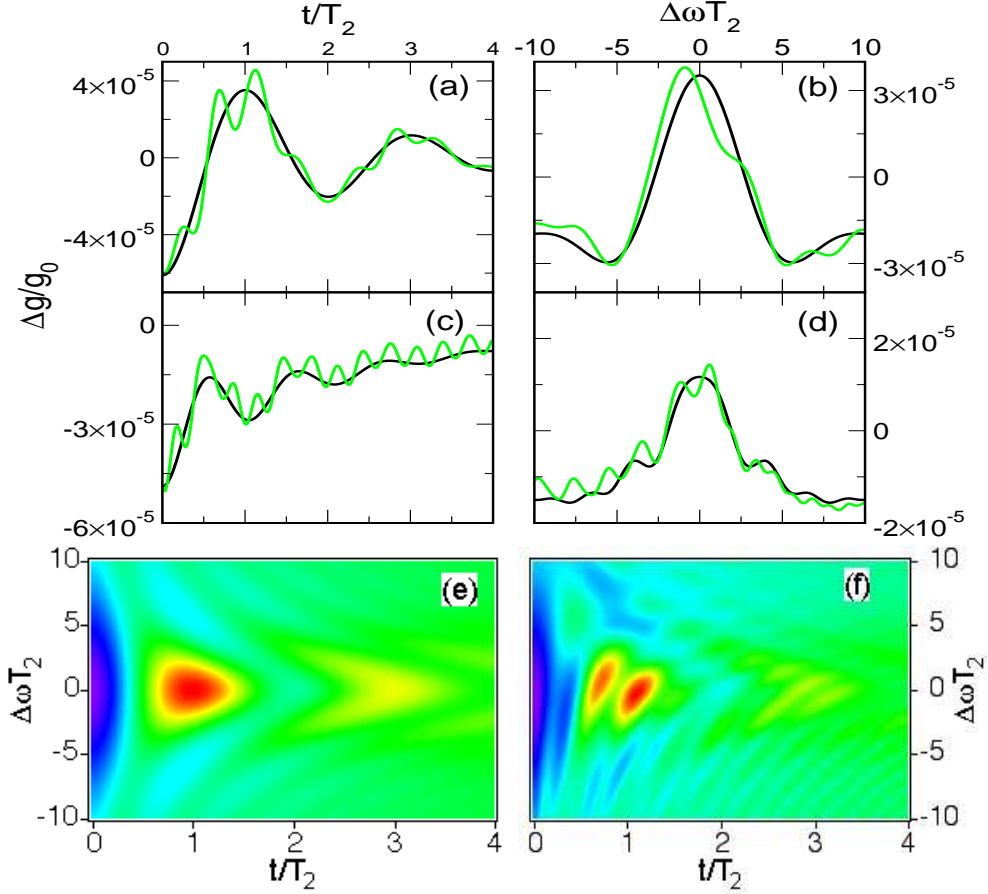
Figure 18: Conductance change spectrum due to transient nutation in the presence of a DC magnetic field H_0 and a strong microwave $\boldsymbol{H}_1 = H_1(\cos\omega t \boldsymbol{e}_x + \sin\omega t \boldsymbol{e}_y)$. $\Delta g/g_0$ as a function of $\Delta\omega \equiv \omega - \omega_0$ and t are plotted in color map for $\lambda = 0$ (e) and $\lambda_1 = \lambda_2 = 0.05$ (f). Panels (a) and (b) describe $\Delta g/g_0$ as a function t/T_2 for $\Delta\omega T_2 = 0$ (on-resonance) and 5 (off-resonance), respectively. Panels (c) and (d) describe $\Delta g/g_0$ as a function $\Delta\omega T_2$ for $t/T_2 = 1$ and 3, respectively. Black lines are from Panel (e) and green lines from Panel (f). $H_1 = 0.18$ G. Other parameters are the same as in Fig. 17.

of graphene-based spintronic devices. Spin injection into graphene was mostly studied in a nonlocal structure, where the spin injection signal (voltage) is probed in a separate circuit than the current injection circuit. By using the AC lock-in technique, the nonlocal spin-injection signal is found to depend strongly on an applied DC-current bias (nonlinear spin transport) in devices with an Al_2O_3 layer between Co and graphene and devices with a transparent interface. Nonlinear spin transport is important in that it allows a thorough comparison between theory and experiment. To date, no systematic theory is available to describe spin injection and nonlinear spin transport in graphene devices. Here we develop such a theory and show that the observed spin transport in both kinds of devices can be consistently modeled by properly describing contact between 3d electrode and 2d graphene, and in particular its spin-dependent transfer lengths, which are short in the transparent-interface devices but long in the devices with Al_2O_3. We find that these transfer lengths largely determine efficacy of spin injection and detection. The concept of spin-dependent transfer lengths introduced in this paper can be extended to other lateral spintronic devices.

9.1   Spin-dependent transfer length

Consider a ferromagnetic electrode on top of a graphene sheet with a current injected from the electrode into graphene (along the z axis). The injected current flows in graphene along the x axis and the width of the graphene sheet, w, is perpendicular to the x axis. The spin-polarized current, I_s, in graphene at x is

$$I_s(x) = w \frac{1}{R_\square^s} \frac{d\mu_s(x)}{dx}. \tag{9.1}$$

Here μ_s is the spin-polarized electrochemical potential and $s = \uparrow$ or $\downarrow$ represents spin polarization. $R_\square^s$ is the graphene sheet resistance for spin s. When the magnetic proximity is neglected, $R_\square^s = 2R_\square$ with $R_\square$ being the sheet resistance of graphene. Because of the current injection, from x to $x + dx$, the current will increase by an amount of

$$dI_s = wdx[\mu_s(x) - \mu_s^f]/\rho_c^s \equiv wdx\Delta\mu_s(x)/\rho_c^s \tag{9.2}$$

where ρ_c^s is the spin-dependent intrinsic contact resistivity, which arises from carrier thermionic emission and/or tunneling and is present even without an interfacial layer between electrodes and graphene, and μ_s^f is the spin-dependent electrochemical potential at the electrode surface next to the graphene ($z = 0$). The value μ_s^f is independent of x because in the electrode the current is presumably along the z direction. From Eqs. (1)

37

and (2), we obtain

$$\frac{d^2\Delta\mu_s(x)}{dx^2} - \frac{\Delta\mu_s(x)}{L_s^2} = 0 \tag{9.3}$$

where $L_s = (\rho_c^s/R_\square^s)^{1/2}$ is the transfer length for spin s, which measures how fast the current transfers from under the contact (lateral) into the contact (vertical). For a magnetic electrode, $L_\uparrow \neq L_\downarrow$, indicating that up-spin and down-spin currents have different paths when injected from the electrode to graphene.

For a finite electrode located at $-a_0 < x < 0$, the general solution to Eq. (3) is $\Delta\mu_s(x) = Ae^{-x/Ls} + Be^{(x+a_0)/L_s}$, and from Eq. (1), it can readily be verified that

$$I_s(x) = I_s(0)\cosh\frac{x}{L_s} + \Delta\mu_s(0)\frac{w}{R_\square^s L_s}\sinh\frac{x}{L_s} \tag{9.4}$$

$$\Delta\mu_s(x) = \Delta\mu_s(0)\cosh\frac{x}{L_s} + I_s(0)\frac{R_\square^s L_s}{w}\sinh\frac{x}{L_s}. \tag{9.5}$$

These are nothing but the transmission line equations of the circuit shown in Fig. 1, where $G = (w/\rho_c^s)$ and $R = R_\square^s/w$. We emphasize that there is a significant distinction between the contact resistance for charge and spin transport. For charge transport the current outside the circuit must be zero. Whereas for spin transport, up-spin and down-spin currents are finite and opposite in sign outside the current circuit, which is in fact the foundation of nonlocal spin detection. The contact resistance obtained from resistance measurements is

$$\frac{1}{R_c} = \sum_s \frac{I_s(0)}{\Delta\mu_s(0)}\bigg|_{I_s(-a_0)=0} = \sum_s \frac{w}{2R_\square L_s}\tanh\frac{a_0}{L_s}, \tag{9.6}$$

which is not scaled with the contact size a_0. Equation (6) suggests that the spin-dependent transfer lengths can be determined by measuring R_c as a function of a_0.

9.2 Transfer length and spin injection

We examine how the spin-dependent transfer lengths affect spin injection. We consider a current of $I_0 + I$ injected into graphene from an electrode at $-a_0 < x < 0$ (the other electrode in the current circuit is assumed at $x = \infty$), where I_0 is a DC bias current and I is a low-frequency AC current, and study the spin-injection signals at the same AC frequency. The DC bias current gives rise to an electric field $E = d\mu_0/dx = I_0 R_\square/w$, where μ_0 is the average (spin-independent) electrochemical potential in graphene. Spin
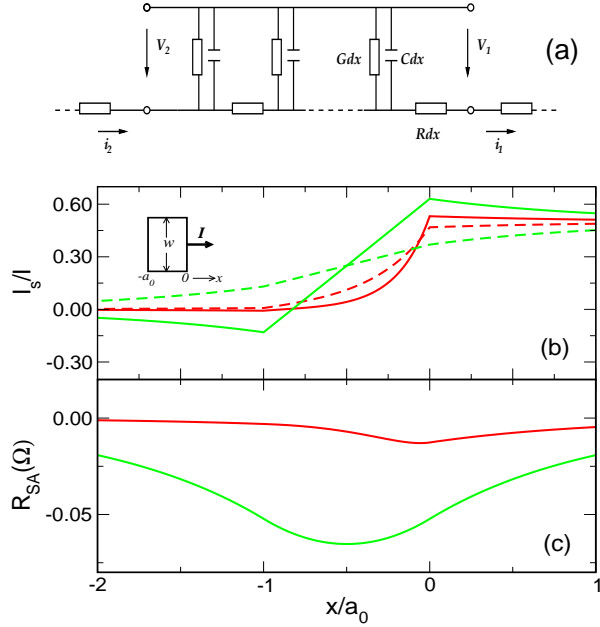
38

Figure 19: Spin-dependent currents (b) and spin accumulation (c) as a function of location in a ferromagnet/graphene structure. The inset of panel (b) shows a top view of the ferromagnet from which an electrical current is injected into graphene and flows to right ($x > 0$). Panel (a) shows an equivalent circuit for an electrode/graphene contact. Solid (dashed) lines in panel (b) describe the up-spin (down-spin) current. Red and green curves correspond to $L_\uparrow = 0.2a_0$ and $5a_0$, respectively. $a_0 = 1\mu$m, $\sigma^f = 1.7 \times 10^5$, $L_f = 50$ nm, $L = 1\mu$m, $(\sigma_\uparrow^f - \sigma_\downarrow^f)/\sigma^f = 0.5$, $R_\square = 1$ kΩ.

transport in graphene was experimentally found to quantitatively follow the spin drift-diffusion equation derived for semiconductors, which can be written in terms of spin-dependent electrochemical potentials,

$$\frac{d^2(\mu_\uparrow - \mu_\downarrow)}{dx^2} + \frac{\nu E}{D}\frac{d(\mu_\uparrow - \mu_\downarrow)}{dx} - \frac{\mu_\uparrow - \mu_\downarrow}{L^2} = 0, \tag{9.7}$$

where ν is the carrier mobility, D is the diffusion constant, E is the applied electric field, and L is the intrinsic spin diffusion length. For ferromagnetic electrodes, the second term in the above equation can be neglected, and Eq. (9.7) becomes the conventional spin diffusion equation.

When $I_0 = 0$, i.e., the linear regime of spin injection, the spin splitting in electrochemical potential, $\mu_\uparrow(x) - \mu_\downarrow(x)$, is proportional to the AC current I, and we define the spin accumulation and the spin injection efficiency as

$$R_{SA}(x) = \frac{\mu_\uparrow(x) - \mu_\downarrow(x)}{I}, \quad \alpha = \frac{I_\uparrow - I_\downarrow}{I}|_{z=0}. \tag{9.8}$$

Figure 19 shows spin-polarized currents, I_s, and spin accumulation, R_{SA}, as a function of x for different transfer lengths. We see that when the transfer lengths are much smaller than the contact size, both the spin current and accumulation concentrate at the inner edge of the circuit. When the transfer lengths are much greater than the contact size, the spin current and accumulation spread across the entire contact.

The injected spin current into the graphene will flow out at the two edges of the electrode. The relative weights of spin currents at the two edges are $P_l = (I_\uparrow - I_\downarrow)_{x=-a_0}/(I_\uparrow - I_\downarrow)_{z=0}$ and $P_r = -(I_\uparrow - I_\downarrow)_{x=0}/(I_\uparrow - I_\downarrow)_{z=0}$, where $P_l + P_r = 1$. In Fig. 20, we depict P_l, P_r and the spin injection efficiency, α, as a function of the transfer length. We see that for $L_s/a_0 < 1$, most of the spin current flows to the inner edge, where the charge current is finite, and the spin injection efficiency is small. As the transfer length increases, the spin currents are equally distributed between the two edges and the spin injection efficiency increases. Since spin injection signals are measured in a voltage circuit next to the current circuit, it is spin accumulation and current at the outer edge, $R_{SA}(-a_0)$ and P_l, that are more important to the measurements. In literature, spin accumulation and spin current are always implicitly assumed to be symmetric at the two edges, which, as shown in Figs. 19 and 20, is valid only when $L_s/a_0 \gg 1$.

9.3   Transfer length and spin detection

To understand spin detection and its dependence of transfer lengths, we consider explicitly only two contacts, $\boldsymbol{p}$ with size c_0 from the voltage circuit and $\boldsymbol{l}$ with size a_0 from the current
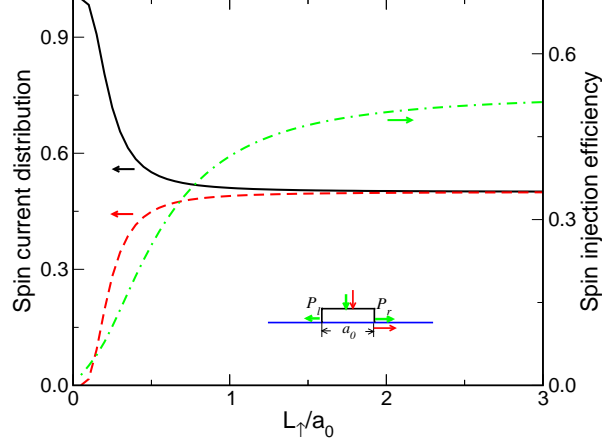
Figure 20: Spin-current distribution at the two edges, P_r (solid line) and P_l (dashed line), and spin injection efficiency α (dot-dashed line) as a function of transfer length. Red (dark gray) and green (light gray) arrows in the inset represent the total current I and the spin current $I_\uparrow - I_\downarrow$, respectively. Parameters are the same as in Fig. 19
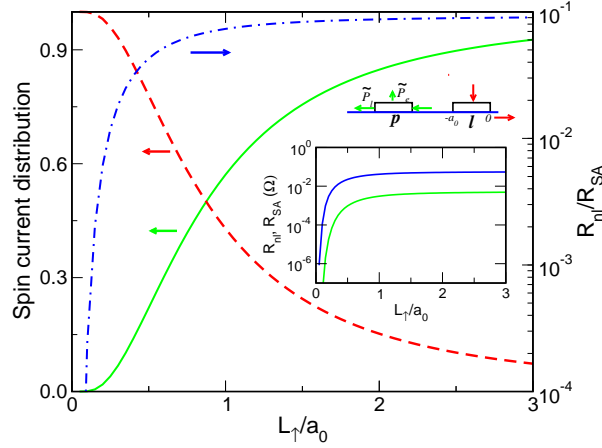

Figure 21: Spin current distribution $\tilde{P}_l$ (solid line) and $\tilde{P}_e$ (dashed line) as well as ratio of the nonlocal resistance and the spin accumulation, R_{nl}/R_{SA}, at $x = -a_0$ (dot-dashed line) as a function of the transfer length. The inset shows nonlocal resistance R_{nl} (green) and spin accumulation R_{SA} (blue). Other parameters are $a_0 = c_0 = 1\mu$m.

circuit, separated by d, as schematically shown in Fig. 21. The other two contacts in the voltage and current circuits can be regarded to be located at $x = -\infty$ and $x = +\infty$. Because of spin injection in the current circuit, a finite difference in electrochemical potential between the two electrodes in the voltage circuit will be developed, $\mu_0^p - w_2$, where w_2 is the electrochemical potential at $x = -\infty$. The nonlocal resistance is defined as

$$R_{nl} = \frac{\mu_0^p - w_2}{I},\qquad(9.9)$$

It is easy to verify that $\mu_0^p - w_2$ flips the sign if electrode $\boldsymbol{p}$ reverses its magnetization. Experimentally the nonlocal resistance is often defined as $R_{nl}^e = \frac{\mu_0^p(p) - \mu_0^p(ap)}{I}$, where $\mu_0^p(p)$ ($\mu_0^p(ap)$) represents the electrochemical potential when the magnetization of electrode $\boldsymbol{p}$ is parallel (antiparallel) with that of electrode $\boldsymbol{l}$. Hence $R_{nl}^e = 2R_{nl}$.

Since electrode $\boldsymbol{p}$ is used for probing the spin accumulation at electrode $\boldsymbol{l}$, it is desired that the measured signal be independent of properties of electrode $\boldsymbol{p}$. Spin currents in electrode $\boldsymbol{p}$ come from the spin currents at electrode $\boldsymbol{l}$, which flows into electrode $\boldsymbol{p}$ at its right edge and then splits into two portions: one into graphene at the left edge with a percentage of $\tilde{P}_l$, and the other into the electrode with a percentage of $\tilde{P}_e$, $\tilde{P}_l + \tilde{P}_e = 1$. We plot in Fig. 21 $\tilde{P}_l$, $\tilde{P}_e$, and R_{nl}/R_{SA} as a function of the transfer length. We find that when $L_s/a_0 > 1$, $\tilde{P}_e$ is small, and both R_{nl} and $R_{SA}(-a_0)$ depend very weakly on L_s with their ratio remaining constant. Whereas for $L_s/a_0 < 1$, $\tilde{P}_e$ is large. Both the nonlocal resistance and the spin accumulation depend strongly on L_s, and the ratio between them also is strongly varying with L_s, suggesting that the measured nonlocal resistance does not accurately reflect the spin accumulation at electrode $\boldsymbol{l}$. This indicates that a "leaking" spin current into the electrode is undesirable for a reliable measurement of spin signals. This resembles measurement of electrical voltage: a good voltmeter must have a very large resistance (small leaking current).

9.4   Nonlinear spin transport: comparison with experiment

To quantitatively model experimental measurements, we consider both the electrodes in the current circuit and the electrode in the voltage circuit that is next to the current circuit, as schematically shown in Fig. 22(a). The experimentally measured signals for the transparent-interface device and for the device with Al_2O_3 are plotted in Fig. 22(a) and Fig. 22(b), respectively. We examine the bias-current dependence of the the nonlocal resistance by solving the spin drift-diffusion equation in Eq. (9.7) with appropriate boundary conditions Eqs. (9.4) and (9.5).

We fix $L_\downarrow/L_\uparrow = 1.3$ and fit the data by adjusting $L_\uparrow$. Good agreement between theory and experiment is obtained when the transfer lengths $L_\uparrow = 40$ nm is used for n-type and

$L_\uparrow = 33.5$ nm for p-type graphene. These lengths correspond to the contact resistance of 43 and 69 Ω for n-type and p-type, respectively, which is in the range of measured contact resistance for the same device and consistent with the observed larger contact resistance in p-type than in n-type. Thus the electron-hole asymmetry for structures with a transparent interface can be attributed to their different contact resistances for n- and p-type graphene. For the device with Al_2O_3, the transfer length used is 800 nm, which corresponds to a contact resistance of 16.3 kΩ for the 90 nm electrode, again consistent with the contact resistance measurements of the same device. We see from panels (c) and (d) that the DC-bias current greatly modifies P_l and P_r with $P_l + P_r = 1$ maintained, i.e., redistributes the spin currents between the two edges. The negative P_l in Fig. 22(d) indicates the sign change of the spin current. The current dependence of P_l and R_{nl}^e have a very similar shape, suggesting that the observed current-dependent nonlocal resistance is due mainly to the electric-field-induced spin current redistribution rather than the change of spin injection efficiency, which depends on the current weakly, as shown in panels (c) and (d).

The above results indicate that the spin-dependent transfer length, which measures the length required for a current to change from lateral in 2d graphene to vertical in a 3d electrode, largely determines efficacy of spin injection and detection. The theory quantitatively explains seemingly conflicting experimental measurements in these devices by different groups and indicates that the observed DC-bias dependence is due mainly to redistribution of the spin current near the ferromagnetic electrode but not to a DC bias-induced change in the spin-injection efficiency, as believed in the literature. The excellent agreement between theory and experiment underscores the necessity of the spin-dependent transfer length in describing graphene and other lateral spintronic device structures. The complete theory and its application to various experimental structures were included in the manuscript, "Transfer lengths and spin injection from a 3d ferromagnet into graphene", which has been accepted by *Phys. Rev. B*.

10 Spin injection into organics

We have collaborated with Prof. E. Nowak from University of Delaware to demonstrate spin injection into organic materials. Magnetoresistance MR measurements for structures with micrometer-thick regioregular, polythiophene rr-P3HT polymer layers between two ferromagnetic contacts indicate a large spin injection. Hole spin transport through the polymer layer leads to a relative MR value in 300 mT fields of 0.3% at 300 K and increasing to 18% at 25 K. Based on our theory of spin transport in organic materials we infer intrinsic spin lifetime and diffusion length to be about 7 ms and 0.4 m, respectively. The
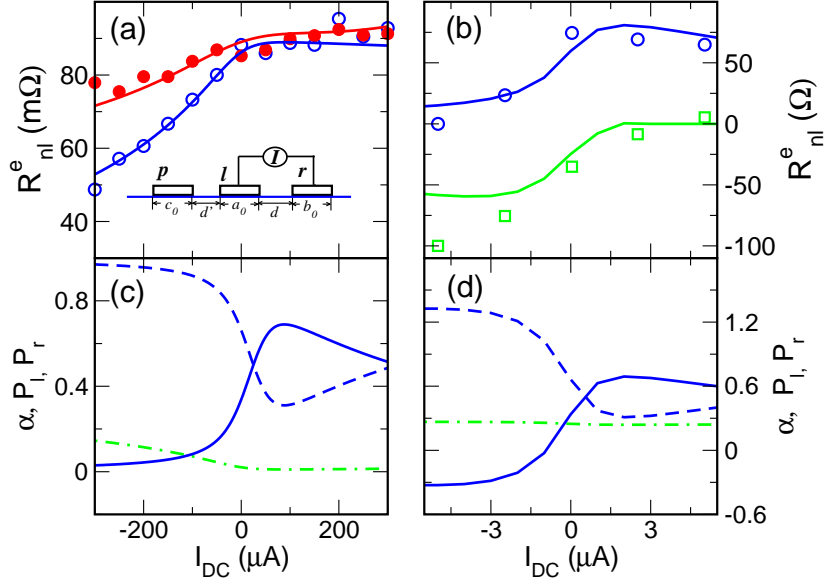
Figure 22: (Color online) Nonlocal resistance for device structures with a transparent interface (a) and with an Al_2O_3 interfacial layer (b) as a function of DC-bias current. Solid (open) circles in (a) are experimental data for the n-type (p-type) graphene when electrode p flips its magnetization. Blue (green) circles in (b) are for experimental signals when electrode l (p) flips its magnetization. Solid lines in (a) and (b) are theoretical results. Panels (c) and (d) are calculated spin injection efficiency α (dot-dashed lines), spin current distribution P_l (solid lines), and P_r (dashed lines) at the left and right edges of electrode l for p-type graphene when the electrodes magnetizations are parallel for the devices in panels (a) and (b), respectively. All three Co electrodes have $\sigma^f = 1.7 \times 10^5$ and $(\sigma^f_\uparrow - \sigma^f_\downarrow)/\sigma^f = 0.5$. The spin diffusion length in graphene is 1 μm.

spin transport coherence length is enhanced by the electric field, as suggested by the theory. leading to an enhancement in MR with increasing applied voltage. This work was published in the paper, "Large magnetoresistance of thick polymer devices having $La_{0.67}Sr_{0.33}MnO_3$ electrodes", *Appl. Phys. Lett.* **95**, 232507 (2009).

Publications

1. Electrically controlled g-factor and magnetism in conjugated metallorganic molecules, Z. G. Yu, *Phys. Rev. B* **78**, 212411 (2008).

2. Microscopic theory of electron spin relaxation in N@C60, Z. G. Yu, *Phys. Rev. B* **77**, 205439 (2008).

3. Fluorescent resonant energy transfer: Correlated fluctuations of donor and acceptor, Z. G. Yu, *J. Chem. Phys.* **127**, 221101 (Communications) (2007).

4. Noninvasive electrical detection of electron spin dynamics at the N atom in $N@C_{60}$, Z. G. Yu, *J. Phys: Condens. Matter* **22** (2010).

5. Transfer lengths and spin injection from a 3d ferromagnet into graphene, Z. G. Yu, J. Baker, and S. Krishnamurthy, *Phys. Rev. B* (in press).

6. Large magnetoresistance of thick polymer devices having $La_{0.67}Sr_{0.33}MnO_3$ electrodes, A. Ozbay, E. R. Nowak, Z. G. Yu, W. Chu, Yijian Shi, S. Krishnamurthy, Z. Tang, and N. Newman, *Appl. Phys. Lett.* **95**, 232507 (2009).

Conference presentations

1. Z. G. Yu, Spin-orbit couplings and spin relaxation in organic electronic materials, 2010 APS March Meeting, Portland, Oregon, March 15-19, 2010.

2. Z. G. Yu, Contact resistances, transfer lengths, and spin transport in graphene structures, 2010 APS March Meeting, Portland, Oregon, March 15-19, 2010.

3. Z. G. Yu, Electrically controlled g factor and magnetism in conjugated metallorganic molecules, 2009 APS March Meeting, Pittsburgh, Pennsylvania, March 16-20, 2009.

4. Yu, Z. G. Fluorescent resonant energy transfer: Correlated fluctuations of donor and acceptor, 2008 APS March Meeting, New Orleans, Louisiana, March 10-14, 2008.

5. Yu, Z. G. Microscopic theory of electron spin relaxation in N@C60, 2008 APS March Meeting, New Orleans, Louisiana, March 10-14, 2008.

6. Yu, Z. G. Spin states and their relaxation in transition-metallorganic self-assembled molecules, 2007 APS March Meeting, Denver, Colorado, March 5-9, 2007.

Recognition of research achievements

1. Our paper, "Fluorescent resonant energy transfer: Correlated fluctuations of donor and acceptor," by Z. G. Yu, *J. Chem. Phys.* **127**, 221101 (Communications) (2007), was the journals third most downloaded article in December 2007.

2. Our research accomplishments were selected in the 2009 Highlights and Achievements from the Office of Basic Energy Sciences, Department of Energy, 2009.